Master Thesis

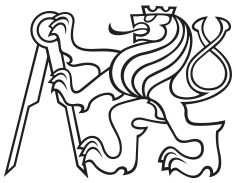

Czech
Technical
University
in Prague

F3

Faculty of Electrical Engineering
Department of Control Engineering

# Structural Tuning of Band Gap in Nanostructured Diamonds

Matúš Kaintz

Supervisor: Antonio Cammarata, Ph.D.
Field of study: Cybernetics and Robotics
May 2022

# Acknowledgements

I would like to thank my supervisor, Dr. Antonio Cammarata, for his patient and professional guidance and for expanding my knowledge in the field of physics and beyond.


# Declaration

Prohlašuji, že jsem předloženou práci vypracoval samostatně, a že jsem uvedl veškerou použitou literaturu.

V Praze, 20. May 2022

# Abstract

The wide range of extreme properties of diamond are making diamond-based materials ideal to build nanoengineered devices with wide applicability in nanophotonic, optomechanics, photovoltaics and electronics. In such applications, it is crucial to understand how to tune the width and the character of the band gap. In the present work, this task is tackled by means of quantum mechanical simulations.

We show that the width of the band gap is determined by the specific local charge distributions in the ion environment around the dopant; in order to control it, we propose how to select suitable dopant atomic types, their concentration and how to impose convenient axial strains on the structure. Moreover, we suggest different ways of acting on the lattice parameters with the aim of changing the character of the band gap.

Due to the generality of our investigation protocol, the presented outcomes can be used to study optical and electronic properties of any material irrespective of their chemical composition or atomic arrangement.

**Keywords:** diamond, doping, band gap tuning, bad gap width, character of the band gap

**Supervisor:** Antonio Cammarata, Ph.D.
Advanced Materials Group,
Department of Control Engineering,
Faculty of Electrical Engineering,
Czech Technical University in Prague,
Prague, Czech Republic

# Abstrakt

Široká škála extrémnych vlastností diamantu robí na ňom založené materiály ideálnymi na výrobu nanorozmerných zariadení so širokou aplikovateľnosťou v nanofotonike, optomechanike, fotovoltaike a elektronike. Pre takéto aplikácie je kľúčové pochopiť ako ladiť šírku a charakter zakázaného pásu. V tejto práci sa na to snažíme prísť pomocou kvantovomechanických simulácií.

V práci ukazujeme, že šírka zakázaného pásu je určená špecifickou lokálnou distribúciou náboja v prostredí okolo dopantu. S cieľom navrhnutia konkrétnej šírky zakázaného pásu navrhujeme ako vybrať vhodný atom dopantu, jeho koncentráciu a ako zaťažiť štruktúru axiálnym napätím. Okrem toho navrhujeme rôzne spôsoby pôsobenia na parametre mriežky s cieľom zmeniť charakter zakázaného pásu.

Vďaka všeobecnosti uplatneného výskumného protokolu môžu byť prezentované výsledky použité na štúdium optických a elektronických vlastností akéhokoľvek materiálu bez ohľadu na chemickú kompozíciu alebo usporiadanie atómov.

**Klíčová slova:** diamant, doping, ladenie zakázaného pásu, šírka zakázaného pásu, charakter zakázaného pásu

**Překlad názvu:** Strukturní ladění zakázaného pásu v nanostrukturovaných diamantech

# Contents

# Figures

# Tables

# Chapter 1

# Introduction

The performance demand for semiconductors is growing, as fast unceasing technological advance leads to a continuous decrease in the size of the devices while increasing their power consumption. [18] Standard semiconductors (e.g., silicon) face many problems such as the inability to work under higher temperatures due to their relatively narrow band gap [14] or under high frequencies due to slow carrier mobility. Many of these problems can be eliminated by using wide band gap semiconductors among which diamond is one of the most exceptional. [18, 75]

Pure diamond is an ultrawide band gap semiconductor with band gap width of 5.47 eV and a wide range of extreme physical properties such as large thermal conductivity ($> 2000\,\mathrm{Wm^{-1}K^{-1}}$), electron and hole mobility ($> 3000\,\mathrm{cmV^{-1}s^{-1}}$), and high breakdown field strength ($10\,\mathrm{MVcm^{-1}}$) [75, 34, 55]. These properties provide tremendous potential for applications in harsh working conditions such as in high-frequency FETs and power electronics, including high-power Schottky diodes [21] and switches [55]. Diamond's qualities seem to be crucial for high-power high-frequency radio signal amplification where travelling-wave tubes are mostly used today, as well as for the high-voltage switches which are predicted to be of particular importance for renewable energy power systems [75]. Furthermore, diamond-based semiconductors are capable of operating at high temperatures while maintaining low conduction and switching losses [55]. Moreover, recent studies are indicating that suitably doped diamond can be essential in the further development of quantum computers, single-photon emitters, high-precision magnetic field sensing devices, and photovoltaics [68, 74, 13, 57].

As each technological application requires a specific band gap size, preferably with direct character so as to improve the efficiency of the device,[52] the gap features of the pristine diamond structure must be modified in order to meet such requirements. The most common method to achieve such desired requirements is by introducing impurities into the diamond structure, mostly by atomic substitution (i.e., doping). Impurities of many types are naturally occurring in diamonds, while nitrogen defects are the most common [36]. Artificial $p$-type doping of diamond with boron has been experimentally proved as possible and efficient [77, 30], while $n$-type doped diamond has been experimentally achieved with nitrogen [59] and phosphorus [7]. Some recent theoretical studies were dedicated to halogen (F, Cl, Br, I ) [78], oxygen[72], lithium [20] and arsenic [69] doping. Other studies investigated on current transport and self-heating effect[44], single-photon emission [46], electron spin-phonon coupling [2] or thermal conductivity [15]. However, the available information is focused on specific aspects of the material preparation and response, while a general understanding of the entangled geometric and electronic properties determining the features of the band gap is missing.

To this aim, in this thesis, we try to uncover the physical phenomena occurring at the nanoscale which determine the width of the band gap and its direct/indirect character (*directness*). In order to identify these phenomena, a quantum mechanical investigation on diamond-based materials with different types of doping atoms (creating both $p$- and $n$-type doped structures) and their concentrations is performed. The study is also expanded by imposing axial tensile strains on the lattice structures. The foundation of this study was laid in my bachelor thesis, which included the computational quantum models of fifteen systems and a preliminary analysis.

At the beginning of the thesis, we describe the basics of the theory behind the quantum mechanical description and the methodology used for the investigation of the electronic structure of many-body systems. Subsequently, we explain the methods and descriptors which we use to analyse the influences of different dopants at varying concentrations. Finally, we propose guidelines on how to select proper dopant atomic types and concentrations to engineer the desired band gap width and character in diamond-based materials, and how to act on the geometric features to finely tune their optical and electronic properties. We believe that the presented investigation protocol can be promptly applied to the study of optical and electronic materials with any chemical composition and atom arrangement beyond those characteristic of the diamond structure.

# Chapter 2

# Theory and Methodology

In this chapter, we will look into the physical theory underlying the quantum mechanical simulations. We will begin by introducing the iconic Schrödinger equation and the numerical methods for solving it, in order to get a physical description of the crystal structures. We will then briefly introduce the direct and the reciprocal lattice; finally, we will discuss the descriptors which we use to analyse the results of the calculations.

## 2.1 The Schrödinger Equation and the Quantum Numbers

*Ab initio* (i.e., from first principles) methods rely on solving the Schrödinger equation [62] to obtain the properties of the system. The most general form of the equation is its time-dependent form

$$i\hbar\frac{\partial\Psi(\boldsymbol{r},t)}{\partial t} = H(\boldsymbol{r},t)\Psi(\boldsymbol{r},t) \tag{2.1}$$

where $t$ is the time, $\boldsymbol{r}$ is the position vector in Cartesian coordinates, $H$ is the Hamiltonian operator representing the total energy of the system, and $\Psi$ is the function solution of the equation carrying the information on the status of the system. If the Hamiltonian does not explicitly depend on the time, the wavefunction can be written as a product of a time- and a space-dependent part; hence, in this case, we seek a solution in the form of $\Psi(\boldsymbol{r},t) = \psi(\boldsymbol{r})\theta(t)$. It can be easily shown that it will yield a solution in the

form of a standing wave, i.e., the dependence of the wavefunction on the time is only the modulation of its phase. In fact, even if the wavefunction oscillates in time, the probability density $|\Psi|^2 = \Psi^*\Psi$ remains the same (the symbol "*" represents the operation of complex conjugation). Therefore, every observable variable remains unchanged throughout time. This will be the case of all the simulations discussed in this work.

The spatial part $\psi(\boldsymbol{r})$ satisfies the following eigenvalue-eigenvector equation known as the time-independent Schrödinger equation:

$$H(\boldsymbol{r})\psi(\boldsymbol{r}) = E\psi(\boldsymbol{r}) \tag{2.2}$$

where $\psi(\boldsymbol{r})$ is the eigenfunction of the Hamiltonian with corresponding energy eigenvalue $E$. A typical example of the Equation 2.2 is the solution for the hydrogen atom. The hydrogen atom is an example of a symmetric spherical Coulombic potential problem; in this case, it is convenient to express the Schrödinger equation in spherical polar coordinates. The wavefunction is then separable into a radial and an angular component, hence the solution is their product:

$$\psi_{nlm}(r, \theta, \varphi) = R_{nl}(r)Y_{lm_l}(\theta, \varphi) \tag{2.3}$$

where $r$ represents the radial distance from the origin of the reference frame, while $\theta$ and $\varphi$ are the zenithal and the azimuthal angle, respectively. $R_{nl}(r)$ is the radial part of the wavefuction and is related to the Laguerre polynomials, while $Y_{lm_l}(\theta, \varphi)$ is the spherical harmonic representing the angular part. The labels $n, l, m_l$ are called *quantum numbers* and uniquely specify the spatial wavefunction, thus the state of the electron. These quantum numbers are a label for the eigenvalues of three commuting operators, i.e., observables that can be measured simultaneously with unlimited precision; such operators are said to form a *complete set of commuting observables*. The quantum numbers and their corresponding operators are defined in Table 2.1.

| Quantum number | Operator | Eigenvalue |
|---|---|---|
| Principal $n$ | Hamiltonian H | $E_n = \frac{E_1}{n^2}$ |
| Azimuthal $l$ | Magnitude of the angular momentum $L^2$ | $L^2 = \hbar^2 l(l+1)$ |
| Magnetic $m_l$ | Projection of the angular momentum along $z$-axis $L_z$ | $L_z = \hbar m_l$ |

**Table 2.1:** Table expressing relations between quantum numbers and eigenvalues of the operators forming the complete set of commuting observables. The $E_1$ corresponds to the negative value of the ionization energy of the hydrogen $E_1 = -13.6$ eV.

The wavefunctions $\psi_{nlm}(r, \theta, \varphi)$ representing individual electrons in the atoms

are called *atomic orbitals*; orbitals with azimuthal quantum number $l = 1, 2, 3, 4$ are also named s, p, d, f orbitals, respectively.

We will study systems at the equilibrium; this implies that the Hamiltonian operator does not depend on the time. Therefore, we will seek the solution of the time-independent Schrödinger equation (Equation 2.2). Unfortunately, only in the case of the hydrogen atom it is possible to find an analytical solution; instead, we will need to solve the Schrödinger equation numerically, by also introducing approximations in the form of the solution and the Hamiltonian. For a better illustration of the complexity of the problem, we here report the generalized Hamiltonian of a system containing $n$ electrons and $N$ nuclei:

$$H = -\frac{\hbar^2}{2m_e}\sum_{i=1}^{n}\nabla_i^2 - \sum_{i=1}^{N}\frac{\hbar^2}{2M_I}\nabla_I^2 + \frac{e^2}{4\pi\epsilon_0}\left[-\sum_{i=1}^{n}\sum_{I=1}^{N}\frac{Z_I}{|\boldsymbol{r}_i - \boldsymbol{R}_I|} + \frac{1}{2}\sum_{i\neq j}\frac{1}{|\boldsymbol{r}_i - \boldsymbol{r}_j|} + \frac{1}{2}\sum_{I\neq J}\frac{Z_I Z_j}{|\boldsymbol{R}_I - \boldsymbol{R}_J|}\right] \tag{2.4}$$

where the electron variables are denoted by lower case subscripts, while the nuclei variables with mass $M_I$ and charge $Z_I$ by uppercase subscripts; $r_i$ and $R_I$ are the electronic and nuclear coordinates, respectively. The Hamiltonian in Equation 2.4 is the sum of five terms: the first two terms correspond to the kinetic energy of the electrons and nuclei, respectively, the third term represents the interactions between electrons and nuclei, the fourth term accounts for electron-electron interaction while the last term stands for nuclei-nuclei interaction. Many methods have been developed to tackle the task of solving the many-body Schrödinger equation; we will briefly describe the most significant ones in the following sections.

## 2.2 The Hartree-Fock Method

The first applied approximation on the path to solving the time-independent Schrödinger equation is the Born-Oppenheimer approximation [8]. The Born-Oppenheimer approximation takes advantage of the great difference in the masses of nuclei and electrons; in fact, even in the case of hydrogen, the ratio is of the order of $1 : 10^3$. Based on this observation, we can assume that the velocities of the electrons are much larger than the ones of the nuclei. Therefore, we can consider as fixed the position of the nuclei and solve the Schrödinger equation for the electrons and nuclei separately, hence with a solution of the form:

$$\Psi(\boldsymbol{r}, \boldsymbol{R}) = \psi(\boldsymbol{r}, \boldsymbol{R})\chi(\boldsymbol{R}) \tag{2.5}$$

where $\psi(\boldsymbol{r}, \boldsymbol{R})$ is the electronic wavefunction and $\chi(\boldsymbol{R})$ is the nuclear wavefunction, while $\boldsymbol{r}$ and $\boldsymbol{R}$ are the coordinates of the electrons and nuclei, respectively. As a result, the main objective in finding the properties of the system is to solve the electronic Schrödinger equation:

$$H_e(\boldsymbol{r}, \boldsymbol{R})\psi(\boldsymbol{r}, \boldsymbol{R}) = \epsilon(\boldsymbol{R})\psi(\boldsymbol{r}, \boldsymbol{R}) \tag{2.6}$$

where $\boldsymbol{R}$ serves as a parameter and $H_e$ is the electronic Hamiltonian for system with $n$ electrons and $N$ nuclei (for description of the individual terms see Equation 2.4):

$$H_e(\boldsymbol{r}, \boldsymbol{R}) = -\frac{\hbar^2}{2m_e}\sum_{i=1}^{n}\nabla_i^2 + \frac{e^2}{4\pi\epsilon_0}\left[-\sum_{i=1}^{n}\sum_{I=1}^{N}\frac{Z_I}{|\boldsymbol{r}_i - \boldsymbol{R}_I|} + \frac{1}{2}\sum_{i\neq j}\frac{1}{|\boldsymbol{r}_i - \boldsymbol{r}_j|}\right]. \tag{2.7}$$

Now, equipped with the Born-Oppenheimer approximation, we can move to the historically first approach to the many-electron problem in the form of Equation 2.6 proposed by Douglas Hartree in 1928 [28]. The Hartree approximation relies on two assumptions:

1. The whole $n$-electron wavefunction can be constructed by multiplication of the $n$ one-electron wavefunctions (i.e., orbitals), thus we can solve them separately.
2. Electrons in an atom are affected by the electrostatic field created by the central potential of the nucleus and the field created by the other electrons.

However, the Hartree approximation treats electrons as distinguishable particles and not as Fermions, i.e., particles with non-integer spin, which have to obey Pauli's exclusion principle [53]. According to Pauli's principle, when two Fermions are exchanged, the wavefunction must change sign, i.e., it has to be antisymmetric. To tackle this problem, Vladimir Fock [23] and John Slater [65] introduced the antisymmetrized $n$-electron wavefunction in the form of *Slater determinant*:

$$\Psi(\boldsymbol{x}_1, \boldsymbol{x}_2, ..., \boldsymbol{x}_N) = \frac{1}{\sqrt{N!}}\begin{vmatrix} \psi_1(\boldsymbol{x}_1) & \psi_2(\boldsymbol{x}_1) & \dots & \psi_N(\boldsymbol{x}_1) \\ \psi_1(\boldsymbol{x}_2) & \psi_2(\boldsymbol{x}_2) & \dots & \psi_N(\boldsymbol{x}_2) \\ \vdots & \vdots & \ddots & \vdots \\ \psi_1(\boldsymbol{x}_N) & \psi_2(\boldsymbol{x}_N) & \dots & \psi_N(\boldsymbol{x}_N) \end{vmatrix} \tag{2.8}$$

where $\psi_i$ is the $i$-th one-electron spin-orbital and $\boldsymbol{x}_i$ corresponds to a merged variable for spin and space coordinates $\boldsymbol{x}_i = (\boldsymbol{r}_i,\ m_{s,i})$. In the section 2.1 we labeled an atomic orbital by means of the three quantum numbers $n, l, m_l$;

however, these quantum numbers define only the spatial part of the orbital. In order to obtain the complete electron wavefunction, we have to include the spin quantum number $m_s$ defined as an eigenvalue of the operator $S_z$, that is the spin angular momentum projected along the Cartesian $z$-axis. Then, the spin-orbital is the product of a spatial and a spin wavefunction of the form $\psi^{m_s}_{nlm_l} = \psi_{nlm_l}\alpha^{m_s}$. The approximation which assumes a solution wavefunction in the form of Equation 2.8 is called *Hartree-Fock* (HF) approximation.

### 2.2.1 The Self-Consistent Field

In the Hartree-Fock approximation, the electronic Schrödinger equation Equation 2.6 for one electron assigned to a spatial orbital $\psi_i(\boldsymbol{r}_1)$ is written as:

$$f_1\psi_i(\boldsymbol{r}_1) = \epsilon_i\psi_i(\boldsymbol{r}_1) \tag{2.9}$$

where $\epsilon_i$ is the $i$-th one-electron orbital energy and $f_1$ is the Fock operator formed by the core Hamiltonian $h$, and the Coulomb $J$ and exchange $K$ operators:

$$f_1 = h_1 + \sum_u [2J_u(\boldsymbol{r}_1) + K_u(\boldsymbol{r}_1)] \tag{2.10}$$

where the sum runs over all the occupied orbitals $u$. The Coulomb operator represents the Coulombic repulsion between the electrons, the exchange operator accounts for the corrections of the energy caused by spin correlation and the core Hamiltonian is the one-electron Hamiltonian for the assigned electron. Each orbital $\psi_i$ is obtained by solving Equation 2.9 with the corresponding Fock operator. However, the Fock operator depends on the exchange and Coulomb operators which in turn depend on all the orbitals of the system, unknown at the beginning of the calculation. Therefore, they are calculated by means of an iterative scheme called *Self-Consistent Field* (SCF). At the beginning of the SCF, a trial set of the $\psi_i$ orbitals is framed and used to create the initial Fock operators, then the HF equations (Equation 2.9) are solved for all the electrons to obtain a new set of orbitals which are the input for the next iteration. The procedure stops when some convergence criterion is reached, e.g., the total energy difference between the two subsequent SCF iterations is lower than a tolerance value specified as an input of the scheme.

The next step to find a reasonable approximation of the solution is to introduce the *basis set*. The basis set is a set of functions used to represent the spatial one-electron orbitals. The $i$-th one-electron wavefunction $\psi_i$ is then represented as a linear combination of such basis functions:

$$\psi_i = \sum_{j=1}^{M} c_{ji}\theta_j \tag{2.11}$$

where $\theta_j$ is the $j$-th basis function from the set containing $M$ functions and $c_{ji}$ is a set of currently unknown coefficients calculated as a result of the SCF. The overall precision of the approximation is dependent on the number of the chosen basis functions and their suitability. Theoretically, a set with an infinite number of bases is needed to achieve the best possible result within the HF method. The suitability of the type of the set depends on the kind of the studied system; [38, 3] in general, the periodic systems would benefit from the plane waves, while molecular systems from atom-centred basis sets as Gaussian- or Slater-type orbitals [38, 3].

The introduction of a basis set, independently suggested by Clemens Roothaan and George Hall (in 1951),[60] paved the way for solving the HF equations as a generalized eigenvalue problem. At the beginning of the procedure, two matrices are formed. The first is the *Fock matrix* $\boldsymbol{F}$, the elements of which are created by integration over the Fock operators $f_i$:

$$F_{ij} = \int \theta_i^*(\boldsymbol{r}_1) f_1 \theta_j(\boldsymbol{r}_1) d\boldsymbol{r}_1 \tag{2.12}$$

where $\theta_i$ are the basis functions. The Fock matrix is the iteratively changed with the change of the fock operators during the SCF procedure. The second matrix to create is the *overlap matrix* $\boldsymbol{S}$, and its elements are created by the overlap integrals of the basis functions $\theta_i$:

$$S_{ij} = \int \theta_i^*(\boldsymbol{r}_1) \theta_j(\boldsymbol{r}_1) d\boldsymbol{r}_1. \tag{2.13}$$

As the set of basis functions is chosen as an input of the calculation and does not change during the iterations, the overlap matrix is calculated only once. The Fock and overlap matrices form the eigenvalue-eigenvector equations known as *Roothaan equations* in the matrix form:

$$\boldsymbol{FC} = \boldsymbol{SC\varepsilon} \tag{2.14}$$

where $\boldsymbol{F}$ is the Fock matrix, $\boldsymbol{S}$ the overlap matrix, $\boldsymbol{C}$ is the matrix of the basis coefficients in Equation 2.11 and $\boldsymbol{\varepsilon}$ is the diagonal matrix containing the energy eigenvalues. The Roothaan equations have a non-trivial solution only if

$$\det |\boldsymbol{F} - \varepsilon_i \boldsymbol{S}| = 0 \tag{2.15}$$

where $\varepsilon_i$ is the energy of the $i$ orbital. The solution of Equation 2.15 is the set of the basis coefficients $c_{ji}$ and orbital energies $\epsilon_i$, while the inputs are the Fock and the overlap matrix. These coefficients are used to obtain a new set of orbitals as shown in Equation 2.11 and subsequently, a new matrix $\boldsymbol{F}$ used in Equation 2.15. The iterative procedure again continues until the demanded stopping criterion is reached. This iterative procedure is summarized in the schematic shown in Figure 2.1. As mentioned above, when the SCF convergence is reached, we obtain the converged HF orbital

energies $\epsilon_i$. Then, we can get the total energy of the electronic system by summing the individual orbital energies:

$$E = \sum_i \varepsilon_i. \tag{2.16}$$

However, this energy represents solely the electronic energy and does not include the contribution emerging from the repulsion between the atomic nuclei. The converged energies together with the coefficients of the basis expansion form the solution of the time-independent Schrödinger equation (Equation 2.2); the solution can then be used to calculate any observable of the system.

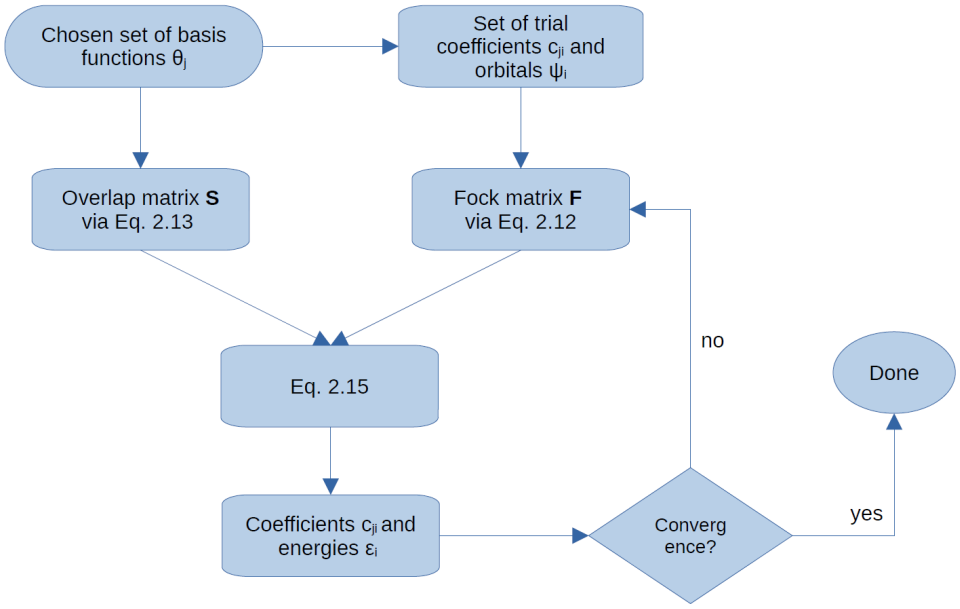


**Figure 2.1:** A schematic representing iterative procedure of the SCF.

### 2.2.2 Limitations of the Hartree-Fock Method

However, even if the Hartree-Fock method considers most of the total energy, including the exchange energy, it does not account for the *correlation energy*. The correlation energy is a summary term describing the instantaneous interaction between the electrons and its subsequent quantum mechanical effect on their distributions. [3] Alternatively, within the Hartree-Fock method, we can define it as a difference between the total energy and the energy calculated by the Hartree-Fock method with the highest possible precision: [38, 45]

$$E_c = E_{tot} - E_{HF} \tag{2.17}$$

where $E_{tot}$ is the total energy of the system without relativistic effects and within the Born-Oppenheimer approximation.

The correlation energy is indeed crucial for a great number of systems; in fact, it has been shown that it plays a fundamental role in the determination of the band gap in diamond-based systems [66]. As the exact expression of the correlation energy is not known, several methods have been developed to improve the HF approach and add the electron correlation into its framework. In general, the methods are based on the expansion of the single Slater determinant into a linear combination of determinants. Such methods are called *post-Hartree-Fock methods*; among the most common ones we can mention the following:

1. Configuration Interaction (CI) [19]
2. Møller–Plesset Perturbation Theory (MP)[47]
3. The Coupled-Cluster Method [43]
4. Multiconfiguration Methods (MCSCF, CASSCF etc.) [70]

These methods add additional accuracy to the solution of the Schrödinger equation; however, they are computationally very demanding and are commonly used only for small systems. To study large structures, which is indeed necessary in our case, we need to look for an alternative approach to solve the many-body Schrödinger equation.

## 2.3 The Density Functional Theory

In parallel with the HF methods, a completely different approach has been developed to solve the Schrödinger equation. In 1927, Llewellyn Thomas and Enrico Fermi independently proposed a way to express the total energy of the electronic system solely in terms of the spatially dependent probability of the electronic density $\rho(\boldsymbol{r})$. They did not provide any proof at that time, although this idea became a precursor for the method now known as *density functional theory* (DFT). The functional is a type of function which takes a function as an input and yields a value as an output. Nearly forty years later,

in 1964, Pierre Hohenberg and Walter Kohn [39] proved that the total energy of the system is a functional of the electron density; in other words, the electron density determines the system wavefunction and all the properties of the system. However, the Hohenberg-Kohn theorem only proves that such a functional exists but, unfortunately, it does not provide any information about its formulation. One year later, Kohn and Lu Jeu Sham presented a set of equations to obtain one-electron wavefunctions (i.e., the Kohn-Sham orbitals). The sum over all the occupied squared Kohn-Sham orbitals can then be used to reproduce the ground-state electronic density:

$$\rho(\boldsymbol{r}) = \sum_{i=1}^{n} |\psi_i(\boldsymbol{r})|^2; \tag{2.18}$$

where $\psi_i(\boldsymbol{r})$ are Kohn-Sham orbitals and $\rho(\boldsymbol{r})$ is the electronic density.

The energy functional $E[\rho]$ of the $n$-electron system is then written as:

$$\begin{aligned} E[\rho] = &- \frac{\hbar^2}{2m_e} \sum_{i=1}^{n} \int \psi_i^*(\boldsymbol{r}_1) \nabla_1^2 \psi_i(\boldsymbol{r}_1) d\boldsymbol{r}_1 - j_0 \sum_{I=1}^{N} \frac{Z_I}{r_{I1}} \rho(\boldsymbol{r}_1) d\boldsymbol{r}_1 \\ &+ \frac{1}{2} j_0 \int \frac{\rho(\boldsymbol{r}_1)\rho(\boldsymbol{r}_2)}{r_{12}} d\boldsymbol{r}_1 d\boldsymbol{r}_2 + E_{XC}[\rho] \end{aligned} \tag{2.19}$$

where the first term represents the kinetic energy of the electrons, the second term corresponds to the attraction between the nuclei and the electrons in the system with $N$ nuclei, and the third term corresponds to the Coulombic interaction among the total charge distribution. The fourth term represents the exchange-correlation energy $E_{XC}$ which deserves the following discussion.

As previously mentioned, to obtain the electronic density it is necessary to find a solution to a system of one-electron Schrödinger equations known as Kohn-Sham (KS) equations. The KS equations for one-electron wavefunction $\psi_1(\boldsymbol{r}_1)$ are written as:

$$\left( -\frac{\hbar^2}{2m_e} \nabla_1^2 - j_0 \sum_{I=1}^{N} \frac{Z_I}{r_{I1}} + j_0 \int \frac{\rho(\boldsymbol{r}_2)}{r_{12}} d\boldsymbol{r}_2 + V_{XC}(\boldsymbol{r}_1) \right) \psi_i(\boldsymbol{r}_1) = \epsilon_i \psi_i(\boldsymbol{r}_1) \tag{2.20}$$

where $\epsilon_i$ are the energies of the KS orbitals and the $V_{XC}$ is the exchange-correlation potential calculated as the functional derivative of the exchange-correlation energy:

$$V_{XC}[\rho] = \frac{\delta E_{XC}[\rho]}{\delta \rho(\boldsymbol{r}_1)}. \tag{2.21}$$

We can notice that the solutions and references for the equations above are entangled. The solution of the Equation 2.20, the KS orbitals $\psi_i$, is the

reference for the calculation of the electronic density$\rho$ in Equation 2.18, in turn $\rho$ is the reference for the Equation 2.18, the solution of which, $V_{XC}$, is again input for the KS equations Equation 2.20. Therefore, as in the Hartree-Fock method, we are forced to use SCF iterative schemes to solve the many-body Schrödinger equation within the Density Functional Theory.

At the beginning of the calculation, the pilot electron density is chosen, usually by superposition of atomic densities, together with the formulation of the exchange-correlation energy. The initial density and $E_{XC}$ are then used to calculate $V_{XC}$ (Equation 2.21) and subsequently the KS orbitals from Equation 2.20. Then the set of orbitals is used to calculate the new electronic density (Equation 2.18) and the total energy (Equation 2.19) which marks the beginning of the following iteration. The iterations are stopped when the convergence criterion is met. The KS orbitals are usually expressed as linear combinations of basis functions, similarly to the HF method; with this choice, the problem transforms into the search for the coefficients of the linear expansion. [38, 3]

The Density functional theory represents a viable alternative to the HF based methods; it takes into account exchange and correlation energy while being less computationally demanding. In fact, with respect to the number of atoms $N$, the DFT formally scales with $\mathcal{O}(N^3)$, HF methods with $\mathcal{O}(N^4)$ while post-HF methods can scale up to $\mathcal{O}(N^7)$. Therefore the DFT represents a viable solution for simulations involving hundreds of atoms. [3]

Finally, we would like to make some remarks on the DFT:

1. It is noteworthy that the first and the third term in Equation 2.20 do not depend on the system, therefore the kinetic $T$ and the electron-electron interaction parts of the Hamiltonian are the same for every system with the same number of the electrons. For this reason they are called *universal operators*. Analogously, we call the first $T[\rho]$ and the third term in the Equation 2.19 *universal functionals*. The remaining terms are non-universal, as they depend on the system under study.

2. The Kohn-Sham orbitals and their energies are mathematical concepts and their physical meaning has been subject matter for discussion. [45]

### 2.3.1 Exchange-Correlation Functionals

The largest source of error in the DFT calculations comes from the fact that the exchange-correlation energy $E_{XC}$ cannot be obtained exactly and it must be approximated. Several approaches to obtain these functionals have been developed, while historically the first and the most simple is the *local density approximation* (LDA).[38, 3] The local density approximation relies on two assumptions: firstly, it treats a general inhomogeneous system as locally homogeneous, by assuming the spatial changes of the electron density to be slow; and secondly, it assumes that the exchange-correlation energy per electron $\epsilon_{XC}$ is the same as in the *homogeneuos electron gas*. The homogeneous electron gas (HEG), [3] i.e., jellium, is a model in which electrons travel through an infinite region of space with a uniform distribution of positive charge to retain overall charge neutrality. The energy in the LDA formulation is then:

$$E_{XC}^{LDA}[\rho] = \int \rho(\boldsymbol{r})\varepsilon_{XC}^{LDA}[\rho(\boldsymbol{r})]d\boldsymbol{r}. \tag{2.22}$$

Many approaches split the exchange-correlation energy into exchange and correlation parts ($\epsilon_{XC} = \epsilon_C + \epsilon_X$) and compute them separately. Indeed, the LDA proceeds in this manner and the exchange energy is expressed exactly by the formula derived by Paul Dirac for the HEG,[38] while the correlation energy has been parametrised in many forms, mostly with the use of quantum Monte Carlo simulations.[38] Although the LDA is very simple and based on a strong approximation, in most cases, e.g., systems with strong bonds, it yields very accurate results. However, it starts to produce errors if the electron density significantly varies throughout the system as in some molecules [38, 3]. In these cases, the gradient correction is introduced into the Equation 2.22 in order to account for the inhomogeneities in the electron density. The simplest of the gradient methods is the *generalized gradient approximation* (GGA). The search for new more accurate exchange-correlation functionals is one of the main goals of today's research efforts regarding the density functional theory. Other more advanced functionals include the *meta-generalied gradient approximation* (m-GGA) [54], which introduces the second derivative (the Laplacian) of the electron density and/or the gradient of the kinetic energy density, and *hybrid functionals*. Hybrid functionals combine the exact exchange energy from the Hartree-Fock method with the exchange-correlation energy from other sources such as GGA, LDA or empirical data. Examples of the most common hybrid functional include PBE0 [1], HSE [29] and B3LYP [4].

In practice, the suitability of the functional formulation depends on the type of the studied system; therefore, the first step before starting the calculation is to check the available literature for suitable candidates. Then, a series of benchmarks must be performed on the system in order to select the energy

functional that best reproduces most of the known properties (if any) of the system of interest. When experimental data on the studied structure is available, the most common benchmark is done by comparing the simulated ground state geometry and the geometry data available from the experiments. The final choice of the formulation is based on the best agreement with the experimental data and it is set as an input for the ab initio simulation software.

## 2.4 Crystal Structure

The focus of our investigation is diamond-derived compounds in the form of a *crystal structure*. A crystal is an ordered state of the matter which is constructed by infinite repetitions of a group of atoms in the space. This group of atoms and their atomic arrangement are called *basis* or *motif*. The *crystal lattice* is a set of mathematical discrete points $\{\boldsymbol{r}\}$ that are defined by the following linear combination:

$$\boldsymbol{r} = u_1\boldsymbol{a} + u_2\boldsymbol{b} + u_3\boldsymbol{c} \tag{2.23}$$

where $\boldsymbol{a}$, $\boldsymbol{b}$ and $\boldsymbol{c}$ are the *translation vectors* or *lattice vectors*, and $u_1$, $u_2$ and $u_3$ are arbitrary integer numbers. The crystal structure is then formed by adding the basis to every point of the space lattice.[37]

### 2.4.1 Bravais Lattice

The volume which includes the atoms in the basis and fills the entire space by replicating itself along the three spatial directions is called *unit cell*. This volume is then defined by the lattice vectors $\boldsymbol{a}, \boldsymbol{b}$ and $\boldsymbol{c}$ in Equation 2.23 as

$$V = |\boldsymbol{a} \cdot \boldsymbol{b} \times \boldsymbol{c}|. \tag{2.24}$$

The choice of the cell basis vectors, and therefore the unit cell, is arbitrary. The unit cell defined by the smallest possible volume is called *primitive unit cell* and it contains only one lattice point. The vectors $\boldsymbol{a}, \boldsymbol{b}$ and $\boldsymbol{c}$ are in this case called *primitive translation vectors*. If the volume enclosed in the unit cell is not the smallest possible, the cell is said to be *conventional*. Similarly to the unit cell, the choice of the primitive cell is not unique and many different algorithms to calculate them exist. The most common primitive unit cell is the *Wigner-Seitz cell*, an example of which is shown in Figure 2.2.

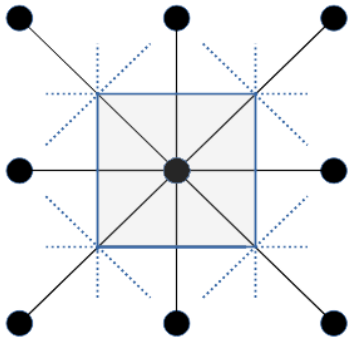

**Figure 2.2:** A simple example of the Wigner-Seitz cell in 2D. The cell is defined by the smallest volume enclosed by bisectors of the line segments connecting the lattice points.

In general, the unit cell may remain invariant under translations or other symmetry operations. The set of symmetries that leaves at least one point unchanged is called *point group*, and may include symmetry operations such as rotations, reflections, rotoinversions, rototranslations (screw axis) etc. [25] In three dimensions, there are 32 different crystallographic point groups; when they are combined with the operation of translation, they form 230 *space groups*, which uniquely define all the possible symmetries of a crystal system.

The lattices may be divided into distinct types, according to their invariance under the translation operation; each of such types is termed *Bravais lattice*, after Auguste Bravais who in 1850 showed that in three dimensions only 14 different lattice types exist, and may be grouped into 7 lattice systems. The Bravais lattice of the diamond-based structures, which are the focus of the present study, is the face-centered cubic one with space group $Fd\bar{3}m$ (no. 227); a schematic of the structure is reported in Figure 2.3.

### 2.4.2 Reciprocal Lattice

As previously mentioned, crystals are periodic systems; therefore, any function representing their physical properties, such as the electron density, is also periodic. It is then convenient to represent such a periodic function by means of the Fourier transform. For this purpose, we introduce the *reciprocal lattice* in the *reciprocal space* as the Fourier transform of the Bravais lattice in the Cartesian space. We sometimes refer to the latter as *direct* or *real* lattice. Analogously to the definition of the direct lattice (Equation 2.23),

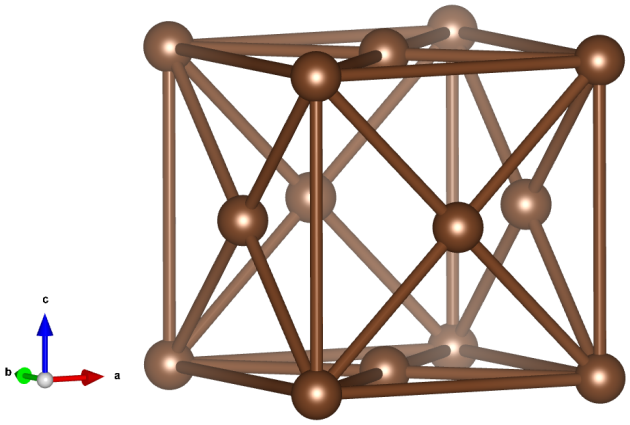


**Figure 2.3:** Schematic representation of the face centered cubic (FCC) Bravais lattice (created by means of the VESTA software [48]).

the reciprocal lattice is defined by:

$$\boldsymbol{g} = v_1\boldsymbol{a}' + v_2\boldsymbol{b}' + v_3\boldsymbol{c}' \tag{2.25}$$

where where $v_1$, $v_2$, $v_3$ are integer numbers and $\boldsymbol{a}'$, $\boldsymbol{b}'$, $\boldsymbol{c}'$ are the reciprocal translation vectors defined as

$$\boldsymbol{a}' = 2\pi\frac{\boldsymbol{b}\times\boldsymbol{c}}{V} = 2\pi\frac{\boldsymbol{b}\times\boldsymbol{c}}{|\boldsymbol{a}\cdot\boldsymbol{b}\times\boldsymbol{c}|} \qquad \boldsymbol{b}' = 2\pi\frac{\boldsymbol{c}\times\boldsymbol{a}}{V} \qquad \boldsymbol{c}' = 2\pi\frac{\boldsymbol{a}\times\boldsymbol{b}}{V}. \tag{2.26}$$

If the vectors $\boldsymbol{a}, \boldsymbol{b}$ and $\boldsymbol{c}$ define a primitive direct lattice then the $\boldsymbol{a}'$, $\boldsymbol{b}'$, $\boldsymbol{c}'$ vectors are also primitive vectors of the reciprocal lattice; thus if the unit cell is primitive in the real space, it is then also primitive in the reciprocal space and is called *first Brillouin zone* (BZ). The reciprocal lattice owns the same symmetries (i.e., space group) as the direct lattice. The Brillouin zone of the FCC lattice, i.e., the lattice of our interest, is reported in Figure 2.4.

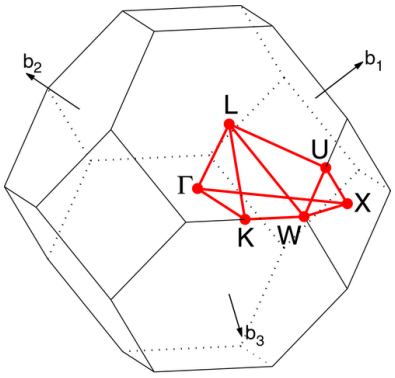


**Figure 2.4:** Schematic representation of the Brillouin zone of the FCC lattice. The red points represent the *high-symmetry points* and the cell enclosed in red is the *irreducible Brillouin zone* (see section 2.5). Reproduced from Ref. [63].

## 2.5 The Bloch's Theorem

Felix Bloch proved that the solution of the Schrödinger equation for periodic potentials, such as in crystals, is in the form:

$$\psi_{\boldsymbol{k}}(\boldsymbol{r}) = u_{\boldsymbol{k}}(\boldsymbol{r})e^{i\boldsymbol{k}\cdot\boldsymbol{r}} \tag{2.27}$$

where $\boldsymbol{r}$ is the position vector in the Cartesian space, $\boldsymbol{k}$ is a vector of the reciprocal lattice, $\psi_{\boldsymbol{k}}(\boldsymbol{r})$ is the one-electron Bloch function or Bloch wave, which is an eigenfunction of the Hamiltonian, and $u_{\boldsymbol{k}}(\boldsymbol{r})$ is a periodic function with the same periodicity of the crystal lattice. The Equation 2.27 shows that the Bloch function is the product of a periodic function $u_{\boldsymbol{k}}(\boldsymbol{r})$ and a phase factor $e^{i\boldsymbol{k}\cdot\boldsymbol{r}}$. Since the phase factor $e^{i\boldsymbol{k}\cdot\boldsymbol{r}}$ does not necessary have the same periodicity as the lattice, neither does the wavefunction $\psi_k(\boldsymbol{r})$. However, the product representing the probability density $\psi_k^*(\boldsymbol{r})\psi_k(\boldsymbol{r})$ preserves the periodicity, hence all the observable properties of the system.

As the Bloch functions are eigenfunctions of the Hamiltonian, by inserting Equation 2.27 into the time-independend Schrödinger equation we obtain:

$$H(\boldsymbol{r})e^{i\boldsymbol{k}\cdot\boldsymbol{r}}u_{i,\boldsymbol{k}}(\boldsymbol{r}) = \epsilon_{i,\boldsymbol{k}}e^{i\boldsymbol{k}\cdot\boldsymbol{r}}u_{i,\boldsymbol{k}}(\boldsymbol{r}) \tag{2.28}$$

$$e^{-i\boldsymbol{k}\cdot\boldsymbol{r}}H(\boldsymbol{r})e^{i\boldsymbol{k}\cdot\boldsymbol{r}}u_{i,\boldsymbol{k}}(\boldsymbol{r}) = \epsilon_{i,\boldsymbol{k}}u_{i,\boldsymbol{k}}(\boldsymbol{r}) \tag{2.29}$$

$$H(\boldsymbol{r},\boldsymbol{k})u_{i,\boldsymbol{k}}(\boldsymbol{r}) = \epsilon_{i,\boldsymbol{k}}u_{i,\boldsymbol{k}}(\boldsymbol{r}) \tag{2.30}$$

Therefore, we can find the energy eigenvalues of the Hamiltonian for each point $\boldsymbol{k}$ in the Brillouin zone separately. In the confined systems, such as ours, for each $\boldsymbol{k}$ there is a discrete set of energies (labelled by $i$). These sets of energies $\epsilon_{i,\boldsymbol{k}}$ for distinct $\boldsymbol{k}$ form what is called the *electronic band structure* [45]. The band structure is elementary for determining the electronic properties of the crystal and we will take a closer look into it later on (section 2.6).

As we are solving the Schrödinger equation in the reciprocal space, we recall that the Brillouin zone owns the same set of symmetries as the direct lattice. The presence of such symmetry operations can be exploited in the search for the solution of the equation. Since the Hamiltonian is invariant under the space group operations, the solution of the Schrödinger equation must be also invariant. First, each Brillouin zone (BZ) contains points to which multiple symmetry operations correspond; we call them *high-symmetry points*. Secondly, it is possible to define the *irreducible Brillouin zone* (IBZ, see Figure 2.4). The IBZ is the smallest possible volume from which it is possible to build the full Brillouin zone after applying the symmetry operations of the crystal. As a result, it is enough to consider only the IBZ when solving the Schödinger equation, as the solution in the full unit cell is obtained by means of the symmetries operations. In fact, the IBZ is always smaller than the BZ

at least by a factor of 2, and in the highest symmetry crystal up to a factor of 48 [45]. The further reduction in the computational load rises from the possibility to consider only a small set of points to sample the BZ. We call these points the *k-points* and one of the most common methods of choosing them is the *Monkhorst-Pack* method [49].

## 2.6 The Electronic Structure

In this section, we will describe the basic quantities that we use to identify the general electronic properties of the system. The first important quantity is the *Fermi level*. The Fermi level is defined as the energy level, if it exists, that has 50 % probability to be occupied at any finite temperature. According to the location of the Fermi level relative to the energy bands, it is possible to determine the electric properties of the material. The material is showing conductive (i.e., metallic) properties when the Fermi level is crossing a nearly continuous set of bands. Indeed, the sets of energy values are discrete, therefore they can be separated by energy regions where no solution in the form of Bloch function exists; these regions are called *band gaps* or *energy gaps*. Then, when the Fermi level lies within such a band gap, or on its lower edge, the material has insulating properties. Depending on the size of the band gap, we may have semiconductor or insulator materials. The two most important bands determining the electronic properties are the bands closest to the Fermi level, i.e., the valence and the conduction band. The term *valence band* indicates the uppermost set of energies fully occupied by electrons at absolute zero temperature, while the term *conduction band* represents the set of energies corresponding to eigenstates for which the electrons are free to move across the material.

The band gap around the Fermi level is the most commonly studied band gap in solid-state physics; its width is defined as the energy difference between the conduction band minimum (CBM) and the valence band maximum (VBM) $\epsilon_{CBM} - \epsilon_{VBM}$. In a conductive system, when the Fermi level lies within the band, the band gap is null. However, in this work, we expand the definition of band gap to conductive systems, for reasons which will be clear later on. As we will see in the following chapter, the Fermi level is located at the highest occupied energy level in all our systems. Furthermore, even in the case of the conductive systems, we will observe the presence of an energy gap between the valence and the conduction band. This allows us to introduce the *generalised band gap* $\Delta$ definition as:

$$\Delta = \epsilon_{CBM} - \epsilon_F \tag{2.31}$$

where $\epsilon_F$ is the Fermi level. With this definition, the band gap assumes

negative values for conductive systems and indicates how deep the Fermi level is in the conduction band. In the case of the systems for which the Fermi level is located at the VBM ($\epsilon_F = \epsilon_{VBM}$), Equation 2.31 corresponds to the standard definition of band gap. The schematic of our definition can be seen in the Figure 2.5. Apart from its width, another relevant property of the band gap is its *directness*: we say that the bandgap is *direct* when the CBM and VBM are located at the same vector $\boldsymbol{k}$, otherwise, we will refer to it as *indirect*.

Another important quantity based on the band structure is the *density of states* (DOS). It is defined as the number of electronic states existing per infinitesimal energy interval $[E,\, E + \delta E]$. As there are no allowed states in the band gap, the latter can be easily calculated from the DOS. We can then define the *total* and the *projected* DOS: the former represents the allowed electronic states of the whole system while the latter corresponds to the contribution of a particular atom or an orbital to the total DOS. The latter is particularly useful for the analysis of the influence of the dopant on the electronic structure, as we can immediately see if the dopant adds states to the top of the valence band or the bottom of the conduction band, thus altering the band gap and the overall properties of the material.

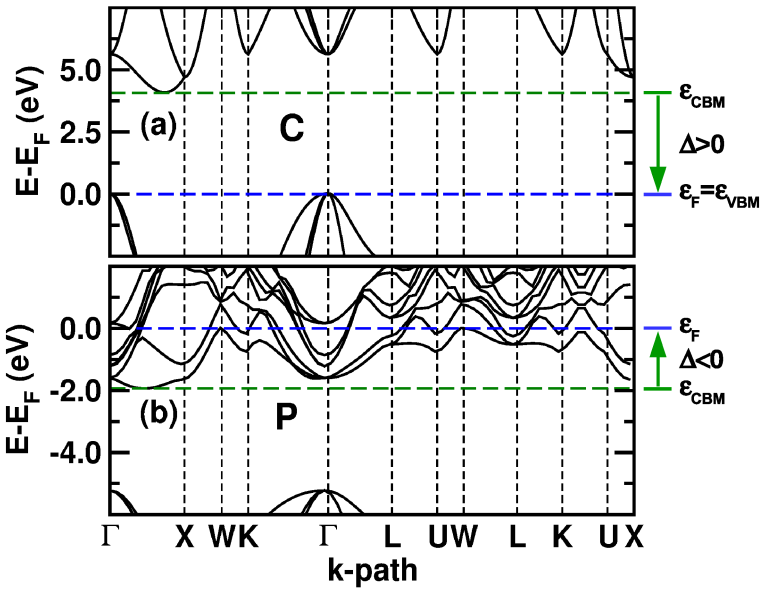


**Figure 2.5:** Schematic representation of the generalised band gap definition. The plot in (a) shows an example of positive band gap, while in (b) we show an example of negative band gap for a conductive system. The green line indicates the conduction band minimum, while the blue line shows the position of the Fermi level.

## 2.7 Calculations

To solve the time-independent Schrödinger equation, we make use of the ABINIT software package [26]. ABINIT is a suite which utilizes the density functional theory to calculate the physical properties of the system. Electron wavefunctions are expanded by means of plane waves basis set. The plane waves ($e^{i\boldsymbol{k}\cdot\boldsymbol{r}}$) represent a natural and computationally efficient choice to represent the Bloch functions. Moreover, the plane wave expansion, therefore the accuracy of the solution, can be easily controlled by a single parameter, which is the plane wave *energy cutoff*. However, the suitable value of this parameter is not known beforehand, hence it must be determined by means of convergence tests. Furthermore, ABINIT takes advantage of the use of *pseudopotentials*.[67] Since the wave function around the nucleus is very steep as a result of strong ionic potential, its representation requires a huge number of plane wave components which would increase the computational load. Based on the assumption that the core electrons are not essential in determining the physical properties of the system, we introduce the *pseudopotentials* which effectively substitute the core electrons and the nucleus. Therefore the number of plane wave components is reduced and limited to the representation of the wavefunctions of the valence electrons. As we consider a large number of structures, some of them containing hundreds of atoms, we perform most of the simulations at the high performance computing centre IT4Innovations, where I have already successfully applied and been granted computational resources for a total of about 1.5 MCPUh (proejct ID: OPEN-21-16).

### 2.7.1 Ground-State Geometry Calculation

The first step on our path to determine the physical properties governing the band gap is to obtain the geometry configuration (i.e., lattice parameters and atomic positions) which realizes the minimum of the energy, that is, the *ground-state* geometry of our systems. The procedure to obtain such a geometry by minimizing the total energy of the system is called *geometry optimization*. During the geometry optimization, we make use of the *Hellmann–Feynman* theorem [22]. The theorem tackles the task by considering how the total energy of the system varies with the change of a parameter $P$:

$$\frac{\delta E(P)}{\delta P} = \left\langle \psi \middle| \frac{\delta H(P)}{\delta P} \middle| \psi \right\rangle . \tag{2.32}$$

The equation can be rewritten to calculate the force acting on the nucleus by choosing its position as a parameter:

$$\boldsymbol{F} = -\nabla E = -\left\langle \psi | \nabla H | \psi \right\rangle . \tag{2.33}$$

Now, we have all the ingredients to calculate the ground-state geometry. Firstly, we will choose the initial geometry according to the experimental data or, in the case that the system does not exist, by choosing the most similar expected geometry. This geometry, together with the choice of the Hamiltonian and other parameters, is provided as an input into the calculation. Then, the total electronic energy is calculated by means of the SCF procedure described in subsection 2.2.1; subsequently, the forces acting on the atoms are calculated via Equation 2.33. The maximum value of the force among all the components is then compared with the convergence criterion. If the maximum is smaller than this criterion then the optimization stops and we declare that the geometry is in its ground-state. However, if the maximum is above the threshold, the positions of the nuclei are altered along the opposite direction of the energy gradient. Afterwards, the total energy of the system is calculated for the new positions of the nuclei and the procedure continues until the convergence is reached. The iteration cycles are sketched in Figure 2.6.

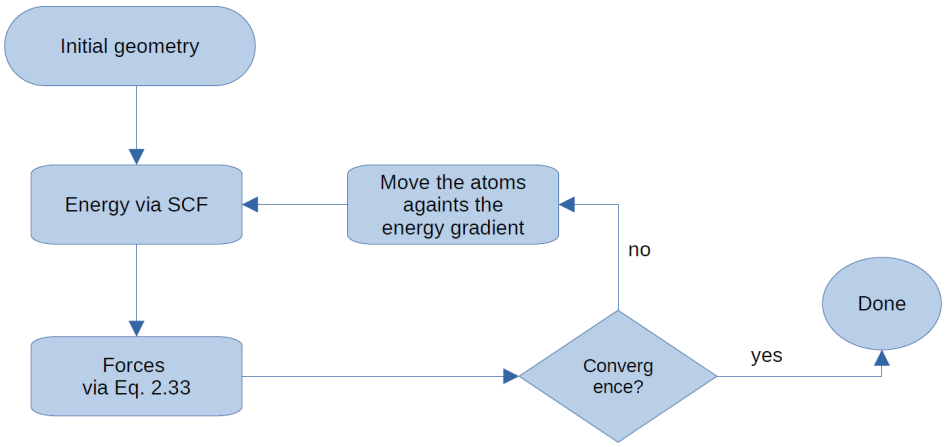


**Figure 2.6:** A schematic representing the *geometry relaxation*.

## 2.8 Descriptors

Once we obtain the ground-state geometry and the relative quantities of our interest (i.e., geometric features, electronic density, band structure and density of states), we can proceed with the data analysis. As previously mentioned, our goal is to identify the physical phenomena which determine the width and character of the band gap; to do so, we will make use of several physical descriptors. In the following subsections, we will briefly introduce some of them, while the generalised band gap has already been introduced in section 2.6.

### 2.8.1 Covalency

Two atoms form a bond with covalent character when they share their electrons in the interatomic region; therefore, we can characterize the covalent character of the bond by analysing the electronic charge distribution along the axis of the bond. To this aim, it is enough to measure the atomic participation to the orbital hybridization generating the electronic density forming the bond. One way to identify such an overlap is to exploit the projected density of states [12]. The centre of mass of an orbital is calculated as:

$$CM^A(n,l,m_l,m_s) = \frac{\int_{\epsilon_0}^{\epsilon_1} \epsilon g^A_{|n,l,m_l,m_s\rangle}(\epsilon)d\epsilon}{\int_{\epsilon_0}^{\epsilon_1} g^A_{|n,l,m_l,m_s\rangle}(\epsilon)d\epsilon} \tag{2.34}$$

where $g^A_{|n,l,m_l,m_s\rangle}(\epsilon)$ is the atomic contribution of the atomic orbital $|n,l,m_l,m_s\rangle$ of the atom A to the total density of states, the orbital being defined by the quantum numbers $n$, $l$, $m_l$ and $m_s$ (section 2.1). We recall here that the total density of states $g(\epsilon)$ is the sum of the orbital contributions over all the atoms:

$$g(\epsilon) = \sum_A \sum_{n,l} \sum_{m_l,m_s} g^A_{|n,l,m_l,m_s\rangle}(\epsilon). \tag{2.35}$$

The choice of the energy interval $[\epsilon_0, \epsilon_1]$ for the integration should include all the bands responsible for the bond creation. The relative position of the centre of mass of the bands corresponding to orbitals of the atoms A and B is then calculated as

$$C_{A,B} = -|CM^A - CM^B| \tag{2.36}$$

which we call the *covalency* of the A–B bond. According to this formulation, the larger this value, the larger the overlap of the bands of the selected orbitals. The greatest possible value of the covalency is zero, which represents the ideal covalent bond.

### 2.8.2 Orbital Polarization

To study the local distribution of the electronic density, we exploit the *orbital polarization* descriptor [27, 11, 9, 10]. The orbital polarization $\mathcal{P}_{i,j}(A,B)$ is defined as

$$\mathcal{P}_{i,j}(A,B) = \frac{n_i(A) - n_j(B)}{n_i(A) + n_j(B)} \tag{2.37}$$

where $n_i(A)$ and $n_j(B)$ are the occupancies of the $i$ and $j$ set of atomic orbitals centered on the atoms $A$ and $B$, respectively. Thanks to this definition, $\mathcal{P}_{i,j}(A,B)$ is an effective and convenient way to measure the excess of charge in the $i$-th orbital relative to the $j$-th orbital.

### 2.8.3 Hirshfeld Charge Analysis

The net atomic charge analyses are commonly divided into two categories [73]. The first category is based on the population analysis of wavefunctions of the system and is dependent on the basis functions; the most notable example from this category is the Mulliken population analysis [50]. The second category is based on the partition of the charge density into what is called *atomic fragments*. The atomic fragments can be overlapping, as in the Hirshfeld's analysis which we use in this study, or non-overlapping as in Bader's approach. The Hirshfeld method [31] partition the charge density at each point among the atoms of the structure according to their contribution to the promolecule (i.e., the reference molecule) density at that point; thus the name "stockholders method". In this manner, the charge dentity of the promolecule $\rho^{pro}(\boldsymbol{r})$ is constructed as a sum of the spherically averaged charge densities of the free atom $\rho^{at}(r)$.

$$\rho^{pro}(\boldsymbol{r}) = \sum_i \rho_i^{at}(\boldsymbol{r}). \tag{2.38}$$

The (pro)molecule in our case is represented by the atoms in the primitive unit cell. Then the sharing function $w_i$ is constructed for each atom $i$, which determines the relative contribution:

$$w_i(\boldsymbol{r}) = \frac{\rho_i^{at}(\boldsymbol{r})}{\rho^{pro}(\boldsymbol{r})}. \tag{2.39}$$

Once the sharing function is calculated, we can find the density of the bonded atom $\rho_i^{b.a.}(\boldsymbol{r})$ from the charge density of the real molecule $\rho^{mol}(\boldsymbol{r})$, obtained for example by ab initio calculations:

$$\rho_i^{b.a.}(\boldsymbol{r}) = w_i \rho^{mol}(\boldsymbol{r}). \tag{2.40}$$

The difference between the density of the bonded atom and the free atom is defined as *atomic deformation density* $\delta\rho_i(\boldsymbol{r})$, which, when integrated with respect to volume $v$, yields the *net atomic charge* $q_i$.

$$\delta\rho_i(\boldsymbol{r}) = \rho_i^{b.a.}(\boldsymbol{r}) - \rho_i^{at}(\boldsymbol{r}) \tag{2.41}$$

$$q_i = -\int \delta\rho_i(\boldsymbol{r}) dv. \tag{2.42}$$

# Chapter 3

# Results and Discussion

In this chapter, we will investigate a variety of doped diamond-based compounds. In the beginning, we report the computational parameters of our simulations which are immediately followed by the analysis of the dopant's influence on the geometry and the electronic structure. Finally, we formulate guidelines on how to tune the width and the character of the band gap. The results reported in this chapter are contained in a scientific article submitted to an impacted journal; at the moment of the thesis composition, the article is under review.

## 3.1 Computation Details

The starting point of our simulations is the pristine bulk structure of the diamond obtained by X-ray diffraction [6]. To identify an optimal set of input parameters we conduct a series of preliminary benchmarks. To this aim, we firstly use a double-loop approach: we calculate the system's energy with different plane wave cutoff values in an inner loop, while the $k$-mesh sampling is changing in the outer loop. Based on the results, we choose the values of parameters for which the energy has an asymptotic trend within $10^{-12}$ eV. In this way, we set the plane wave energy cutoff to 1633 eV and the energy cutoff for the projected augmented wave double grid to 3265 eV. The sampling of the Brillouin zone is done within the Monkhorst-Pack scheme [49] and differs with the size of the unit cell; the optimal values are reported in Table 3.1.

| Multiplicity of the supercell | k-mesh |
|---|---|
| $1 \times 1 \times 1$ | $21 \times 21 \times 21$ |
| $2 \times 2 \times 2$ | $11 \times 11 \times 11$ |
| $3 \times 3 \times 3$ | $7 \times 7 \times 7$ |
| $4 \times 4 \times 4$ | $5 \times 5 \times 5$ |
| $5 \times 5 \times 5$ | $5 \times 5 \times 5$ |

**Table 3.1:** $k$-mesh for different sizes of the supercells.

Then, we optimize the experimental structure with different energy functionals and choose the optimal one as explained in subsection 2.3.1. For all our simulations, we choose the GGA WC [76] functional, as it reproduces the lattice parameters and the band gap with the highest accuracy. The stopping criterion for the SCF cycles is set by means of the energy difference between two subsequent iterations to $10^{-11}$ eV. For our analysis, we need to obtain the geometries which realize the ground state energy; therefore the geometry optimization is stopped only after the maximum component of the forces acting on the atoms is smaller than $5 \times 10^{-6}$ eV/Å. The length of the lattice parameter of the optimized diamond structure is 3.5612 Å, which is consistent with the experimental value of 3.567 Å [6] and has the symmetries of the face-centred cubic spacegroup $Fd\bar{3}m$ (no. 227). The calculated band gap size is 4.14 eV, in agreement with already reported DFT calculations [24]; nonetheless, it is narrower than the experimental value of 5.47 eV [75, 34]. In fact, it is well-known that the DFT calculations tend to underestimate the size of the band gap in periodic systems [5]; however, we are interested in relative variations of the physical features which are not affected by shifts of the band energy.

To be able to identify the features governing the band gap we introduced nine different dopants into the pristine diamond structure, one at a time. Initially, we considered five p-block dopants, namely Al, B, N, P and Si; subsequently, we expanded the study by considering four transitional metal atoms, specifically Cr, Sc, Ti and V, in order to verify our hypotheses. With such a variety of dopants, we are able to create both $n$- and $p$-type diamond, and identify the suitable doping candidates throughout the periodic table far beyond those considered in our study. The aluminium, boron and scandium atoms are *electron acceptors* as their valence shell contains fewer electrons than that of carbon, thus creating a $p$-type diamond structure. On the other hand, $n$-type diamond is created by doping with nitrogen, phosphorus, chromium and vanadium as they are electron donors, i.e., they have more valence electrons than carbon. Silicon and titanium have the same number of valence electrons as the carbon; however, they act as $p$-type dopants: in the following sections, we will try to uncover why. The doped structures are

modelled by three-dimensional replication of the pure diamond's unit cell and by substituting one carbon atom with a dopant. We consider $2 \times 2 \times 2$, $3 \times 3 \times 3$, $4 \times 4 \times 4$, and $5 \times 5 \times 5$ replicas (*supercells*); in this way, we consider 16, 54, 128 and 250 atoms in our models, respectively, and thus simulate dopant concentrations at 6.25%, 1.85%, 0.78% and 0.4%. In the following text, we will refer to a specific doped system as X-$n$, where X is the kind of the doping atom and $n$ is the three-dimensional multiplicity of the supercell. As an example, when we mention the Al-2 model, we mean the supercell created by $2 \times 2 \times 2$ multiplication of the pristine diamond unit cell and doped by one aluminium atom. Examples of the primitive and conventional unit cells of the X-3 and X-4 systems are shown in the Figure 3.1.

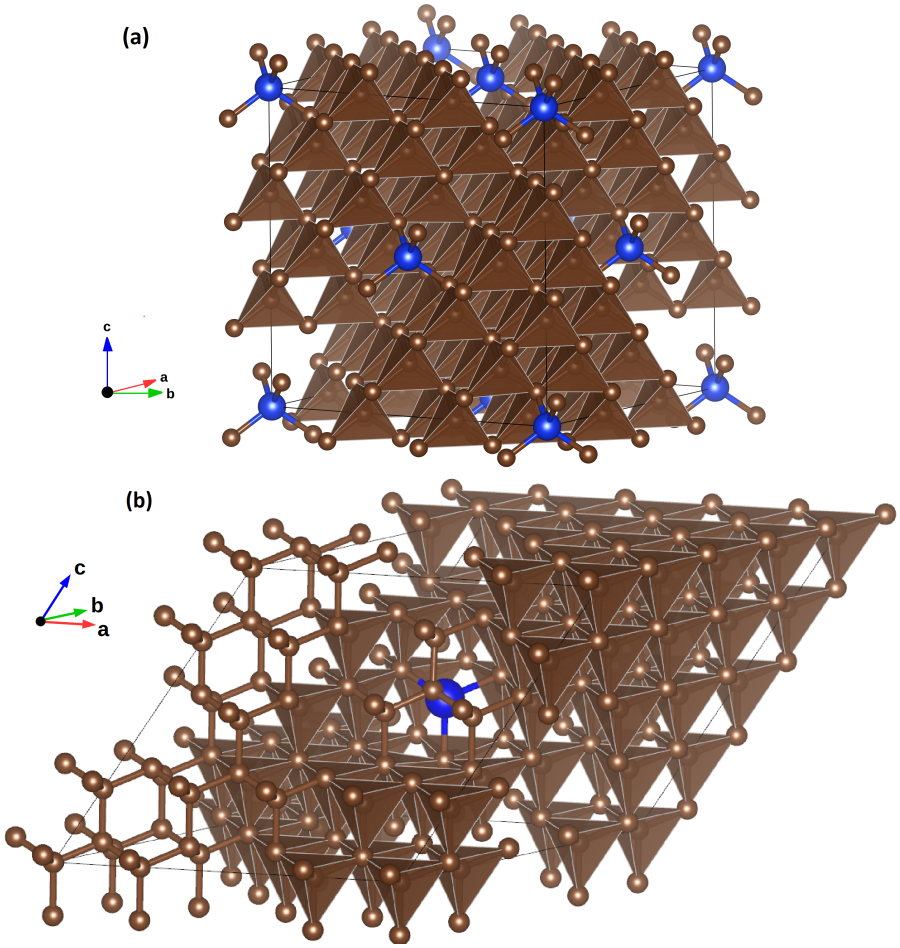


**Figure 3.1:** Examples of the unit cells simulating X-3 (a) and X-4 (b) (concentration 1.85 % and 0.78 %) systems with corresponding lattice vectors. The figure (a) represents the conventional unit cell corresponding to the face centred cubic lattice, while the figure (b) shows the primitive unit cell, used in calculations. Blue and brown spheres represent dopant and carbon atoms, respectively. The grey line denotes the boundaries of the unit cell.

## 3.2 Geometry Analysis

The first step of our analysis is to investigate the influence of the dopant on the pristine structure. We observe that, regardless of the size of the dopant and irrespective of its doping concentration, each dopant is surrounded by four first neighbours forming a regular tetrahedron. As a result, this kind of substitutional doping preserves the face centred cubic Bravais lattice of the pristine diamond (Figure 3.1); all the considered doped models own the symmetries of the same space group $F\bar{4}3m$ (no. 216), which is different from the pristine structure as a consequence of the introduction of the dopant atom.

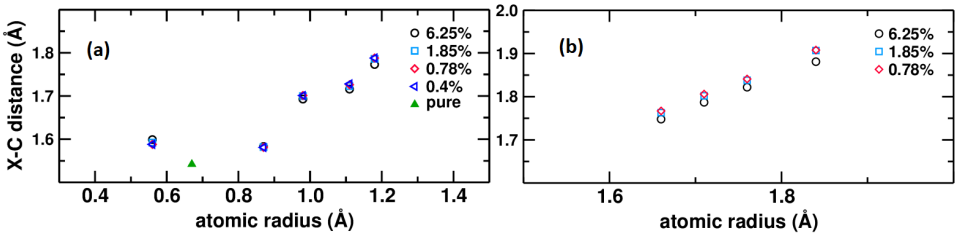


**Figure 3.2:** Interatomic distance between the dopant and the neighbouring carbons as a function of the atomic radius of the dopant. Figure (a) contains the p-block dopants while figure (b) the transition metals. The "pure" label represents the C-C distance in the pristine structure.

In order to analyse the changes in the initial geometry induced by the presence of the dopant, we compare the X-C bond length as a function of the atomic radius, i.e., the dopant type (Figure 3.2). We can clearly notice that the dopants with larger radii induce larger lattice distortions in their immediate vicinity (Figure 3.2a); such a trend is clearly visible in the case of the transition metals (Figure 3.2b). The largest distortions are then found in the cases of aluminium and scandium, the latter being the dopant with the largest radius in our study. The concentration has minor effects on the X-C distance; the largest difference between the concentrations is observed between the X-2 and the other systems. In the case of 6.25 % (X-2) concentration, the coordination shells of the doping atoms are close enough to experience the influence of each other on their local environments; this causes a slightly smaller X-C distance when compared to other concentrations. As expected, such a difference in the distance is then proportional to the atomic radius of the dopant. On the other hand, the lattice is capable to attenuate such distortions over longer distances, that is, at concentrations below 1.85 % (X-3 models). Therefore, in these cases the dopants behave as isolated defects, thus realizing the same X-C distance. To sum up, we can conclude that the only effect which the atomic type of the dopant has on the system geometry

is to determine the magnitude of the distortions in its first neighbouring shell, i.e., the X-C interatomic distance. We then expect that this will determine the degree of hybridization between the orbitals participating in the X-C bond, thus the features of the band gap.

## 3.3 Electronic Structure Analysis

We will now proceed with the analysis of the electronic structure. To this aim, we will compare the band structure, the band gap and the density of states of the doped and pristine structures. We then deduce the effects of the atomic types of the dopants and their concentration on the electronic properties of the system. We point out that, in this section, we will distinguish between the terms *band* and *energy* gap for the clarity of the analysis. With the term energy gap, we will refer to any region where no bands exist, while with the band gap we refer specifically to the energy gap about the Fermi level.

The first step of our analysis is to compare the electronic band structures calculated along the standard piece-wise linear path joining the high-symmetry points in the irreducible Brillouin zone [63]. As the band structures at different concentrations with the same atomic type share very similar features, we report only the band structures of the highest and lowest concentrations for comparison. This corresponds to the X-2 and X-5 systems doped with p-block dopants (Figure 3.12) and to X-2 and X-4 systems doped with transition metals (Figure 3.13) since the X-5 models where X is a transition metal have not been considered.

Firstly, we analyse the $p$-type structures; we remind that these are formed by Al, B, Si, Sc and Ti doping. We observe that the concentration has a major influence on the size of the band gap; with lowering concentrations the band gap size increases (Figure 3.3). We then analyse the differences between the p- and d-block dopants. The p-block dopants contribute to the band gap with states lying at the edges of the band gap (Figure 3.12); on the other hand, states of the d-block dopants are found within the gap including the Fermi level (Figure 3.13). Moreover, after doping, the valence band maximum is no longer located at the $\Gamma$ point as it is in the pristine structure and in the structures doped by p-block dopants.

To obtain an understanding of the origin of such phenomena, we need to analyse the projected density of states. The $p$-type dopants are electron acceptors, therefore the electron occupying the top of the valence band of

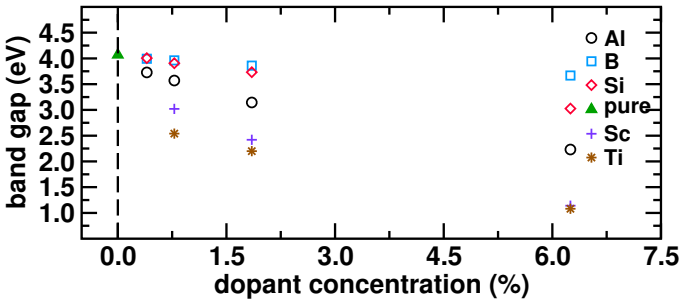


**Figure 3.3:** Band gap width as a function of the dopant concentration in $p$-doped systems.

the pure structure is shifted to the dopant states. Interestingly, the Al-5 system is already showing the separation of the acceptor states from the main bulk of the valence band, which can be seen as a minor energy gap in the valence band close to the Fermi level (Figure 3.14b). We see that, indeed, irrespective of the atomic type and concentration, the dopants are adding states to the top of the valence band (Figure 3.14). In the structures doped by the transition metals, we find that the band in the middle of the band gap is formed purely by the $d$-states of the doping metals (Figure 3.15). The introduction of the acceptor states gives rise to the alteration of the whole energy spectrum with the effect of narrowing the band gap via a shift of the Fermi level. Moreover, as expected, we observe that the contribution of the dopant to the total density of states near the Fermi level diminishes with lowering concentration.

We proceed by investigating the $n$-type systems, i.e., doped by electron donors (N, P, V, Cr). We can immediately notice that the Fermi level is now located in a region of the DOS which can be identified as the conduction band of the pristine diamond (Figure 3.12); this phenomenon is caused by the excess electron introduced into the structure by the dopant atom. Such excess of the electrons needs to be accommodated in the pristine band structure. However, the unoccupied states with the lowest energy lie already in the conduction band; thus the electrons have no choice but to occupy these states. The Fermi level is shifted according to the position of the uppermost occupied state. As the Fermi level is crossing the set of the bands, the thermal excitation is enough to promote the electron to the conduction band, thus the systems are conductive (i.e., metallic). As we mentioned in the theory part section 2.6, the energy gap below the Fermi level is still existent. In the structures doped by p-block dopants, the band dispersion enclosing the energy gap is similar to the pristine structure or the $p$-doped structures. Interestingly, in the cases doped by transition metals (TM) the $n$-doped systems have the former band gap split into three separate energy gaps (Figure 3.13). As we did for the $p$-doped case, in order to understand the origin of the conductivity of the $n$-doped models we analyse the projected density of states. Analogously to the $p$-doped structures, we find that the bottom of the conduction band is

mainly formed by the states introduced by the donor atom (i.e., donor states) (Figure 3.14). This is in good agreement with both our discussions: the effect of doping with a donor is to add electrons to the bottom of the conduction band of pristine structure, while leaving the band dispersion nearly unaltered. Again, similarly to the *p*-type systems, the decreasing concentration has the effect of reducing the donor contribution to the formation of the states in the vicinity of the Fermi level. It is worth noticing that the donor states of the N-5 system are already separated from the conduction band by a minor band gap. In TM-doped structures, we find that both set of bands introduced into the former band gap (i.e., located between the main bulks of the valence and conduction bands) are formed by *d*-states of the metal. Then, the Fermi level crosses the set of bands with the higher energy of these two.

To dive even into more details, we study the individual orbital contributions by considering the resolved projected density of states (Figure 3.16 and Figure 3.15). We observe that, irrespective of the kind of the dopants, both *p*- and *n*-type structures show the following common features. The $p_x$ and $p_y$ orbital projection centred at the atomic site of the dopant as well as at the atomic site of the neighbouring carbons are degenerate in both p-block-doped structures. We can clearly distinguish that the $p_x$ and $p_y$ orbitals of the dopant contribute predominantly to the top of the valence band, while the $p_z$ orbital is predominant in the conduction band in the p-block-doped systems. As expected, all the tree *p*-orbitals fully hybridise with the orbitals of the neighbouring carbons. In the TM-doped systems, we observe two pairs of degenerate *d*-orbitals centred at the atomic site of the dopant, namely $d_{xy}$, $d_{yz}$ and $d_{xz}$, $d_{x^2-y^2}$. Similarly to the p-block doped structures, we find that the pair $d_{xy}$, $d_{yz}$ contributes mostly to the top of the valence band, while $d_{z^2}$ is predominant in the conduction band, and the $d_{xz}$, $d_{x^2-y^2}$ pair is present in both bands.

To sum up, the results presented in this section show that the pristine structure is capable of accomodating the variation of the electrons in a way that the dopant's presence does not dramatically alter the features of the electronic band dispersion nor the general profile of the density of states. The main effect is the change of the position of the Fermi level relative to the conduction band minimum; the electron acceptors reduce the width of the band gap, while electron donors make it disappear or at least reduce it to a negligible size as in the N-5 system. Such behaviour is present in all the systems irrespective of the dopant concentration; however, the concentration indeed modulates the effect of the atomic type on the position of the Fermi level. Finally, we notice that the atomic orbitals of the dopant mainly oriented along the *z*-axis in our settings are predominant in the conduction band; the consequences of this fact will be discussed in the following section.

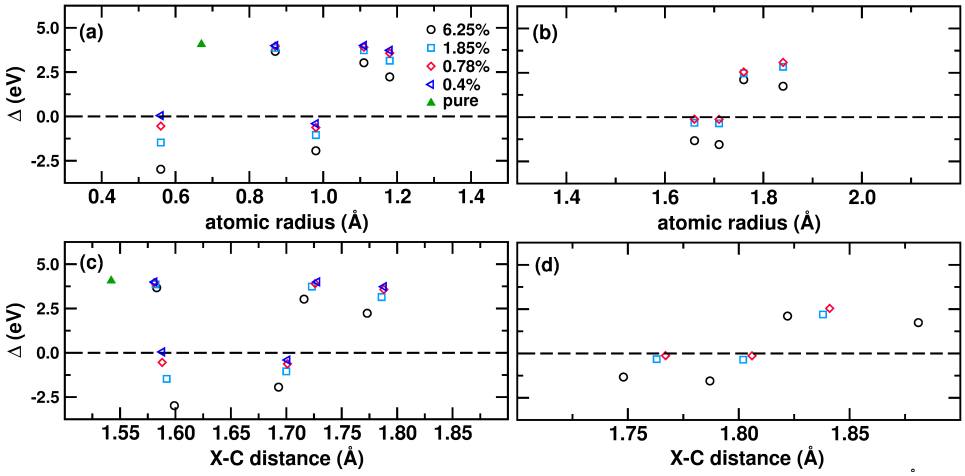


**Figure 3.4:** Generalized band gap width as a function of (a, b) the atomic radius and (c, d) the dopant-carbon distance. The green triangle indicates the pure diamond. The plots on the left represent structures doped by p-block dopants while the the plots on the right by the transition metals. The legend is common to all the plots.

## 3.4 How to Engineer the Width of the Band Gap

We here recall the definition of the generalised band gap $\Delta$ that can be found in section 2.6: $\Delta = \epsilon_{CBM} - \epsilon_F$. From now on, when we mention the band gap we refer to this definition. This descriptor will guide us in the study of the details of the local electronic distribution in the vicinity of the dopant and its first neighbouring carbon atoms. The local electronic distribution is determined by the degree of orbital hybridization between the two atoms contributing to the bond. In turn, the hybridization is regulated by the orbital overlap, which goes hand in hand with the interatomic distance between the atoms, the latter mainly governed by the atomic radii. For this reason, we will firstly take a closer look at the last two mentioned features.

We notice that when we fix the dopant concentration, the positive (negative) band gap size increases (decreases) with the increasing interatomic distance X-C, thus with the increasing atomic radius (Figure 3.4). On the other hand, when we fix the atomic radius (i.e., atomic type) or the X-C distance, we observe that the sizes of the bad gap are spread around their average, while such a spread is determined by the concentration and is of the order of 1.3 eV (Figure 3.4c). As a consequence, this implies that the spatial extension of the dopant electron distribution (atomic size) and the orbital overlap (X-C distance) subtly determine the electronic structure near the Fermi level, while the concentration finely tunes such an overlap. In order to study these features in a more detailed way, we calculate the Hirshfeld charges and the

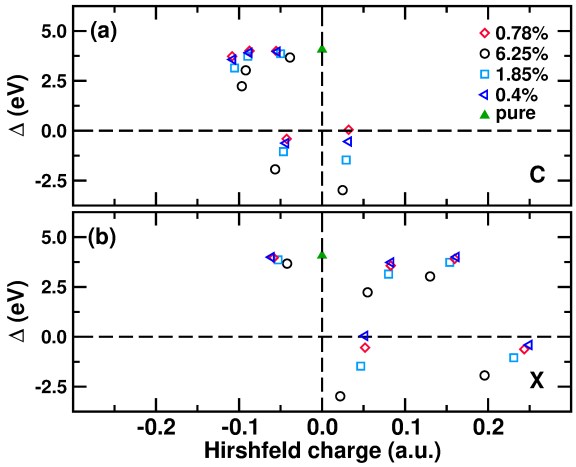


**Figure 3.5:** Generalized band gap as a function of the Hirshfeld charges on the (a) carbon atoms in the first coordination shell of the p-block dopant and (b) on the dopant atom.

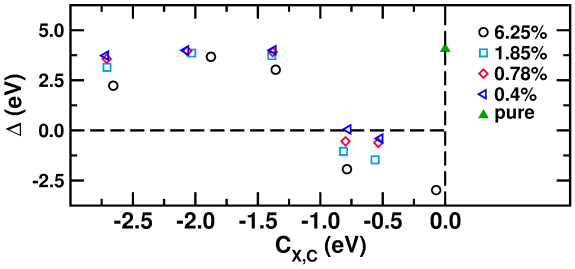


**Figure 3.6:** Generalized band gap as a function of the X–C bond covalency at the different p-block dopant concentrations. By definition, the maximum covalency value is 0 eV, while the lower the value, the more ionic the bond.

bond covalency $C_{X,C}$ defined in quantum mechanical terms of the projected density of states; the complete definition of both descriptors can be found in section 2.8.

As previously mentioned, the dopant atom is surrounded by four neighbouring carbon atoms with equal bond X-C distances, thus forming a regular tetrahedron. In such a symmetric environment these four carbons are electronically equivalent; this can be noticed by investigating their atom-projected density of states, which overlaps across the whole energy spectrum of the Hamiltonian. As a result, it is enough to analyse the Hirshfeld charge and covalency of only one of the dopant's neighbouring carbons. We do not find any regular trend for the band gap size as a function of the Hirshfeld charges on the dopant or its first neighbours (Figure 3.5). This result was expected, as the band gap size is determined by the subtle details of the local charge density distribution; however, such details are lost when we consider the atomic charge obtained by partial integrations of the total charge density

(subsection 2.8.3). Nonetheless, the bond covalency shows promising results: it seems that, when the covalency exceeds a certain threshold, the band gap becomes negative irrespective of the concentration (Figure 3.6). The only exception is presented by the pure diamond structure where the covalency is equal to zero $C_{C,C} = 0$, thus representing the perfect covalent bond. As a consequence, we can conclude that the X-C covalency is a promising parameter to engineer the value of the band gap.

These results imply that the degree of overlap between the orbitals of the dopant and the neighbouring carbons plays a fundamental role in determining the width of the band gap. To analyse such an overlap more in detail we make use of the orbital polarization descriptor $\mathcal{P}_{i,j}(A, B)$ (subsection 2.8.2). We here recall that $i$ and $j$ represent the sets of atomic orbitals centred at the site of the atom A and B, respectively. To simplify the notation, we will use the symbol $\mathcal{P}_{i,j}(A)$ when comparing the charge in the orbitals of the same atom ($A = B$). We adopt atom-centred hydrogen-like wavefunctions to calculate the orbital polarizations centred at the site of the substituent and the neighbouring carbon atoms. With this approach, we partition the electronic density according to the spatial character of the orbital and examine the possible preferential charge distributions in the local environment of the dopant. We begin this analysis by considering the orbital polarizations of the p-block dopants and their first neighbours among their own orbitals. As we discussed, the $p_x$ and $p_y$ orbitals are degenerate, hence $\mathcal{P}_{p_x,p_y}(C) = 0$, $\mathcal{P}_{p_x,p_y}(X) = 0$, $\mathcal{P}_{p_x,p_z}(C) = \mathcal{P}_{p_y,p_z}(C)$ and $\mathcal{P}_{p_x,p_z}(X) = \mathcal{P}_{p_y,p_z}(X)$ in all our models. We do not find any regular trend of the band gap size as the function of $\mathcal{P}_{p_x,p_z}(C)$ (Figure 3.7a). On the other hand, it seems that a positive value of $\mathcal{P}_{p_x,p_z}(X)$ ($= \mathcal{P}_{p_y,p_z}(X)$) at the dopant site determines a positive value of the band gap, with an exception found for the N-4 system (Figure 3.7b). We now proceed with the comparison of the relative occupation of the $p_x$ ($= p_y$) orbital of the dopant and the surrounding carbon (C) atoms. In this way, we obtain details about the spatial distribution of the charge along the bond axis. We observe that irrespective of the concentration, the positive (negative) band gap size seems to increase (decrease) with $\mathcal{P}_{p_x,p_x}(X, C)$, with a maximum positive value found for the undoped case (Figure 3.7c). By conducting the same investigation on the $p_z$ orbital we find that band gap seems to increase when $\mathcal{P}_{p_z,p_z}(X, C)$ approaches zero, while the negative band gap values are found for positive values of the polarization (Figure 3.7d).

The three $\mathcal{P}_{i,i}(X, C)$ polarizations determine the covalency of the bond since they are the consequence of the orbital overlap of the dopant electron density and the densities of the neighbouring carbons. In fact, large negative $\mathcal{P}_{i,i}(X, C)$ values indicate a depletion of the charge at the atomic site of the dopant and a consequent accumulation at the bonding carbon site along the bond axis, this being signature of a bond with ionic character (Figure 3.8). We can then conclude that the lower (higher) the $\mathcal{P}_{i,i}(X, C)$ the more ionic

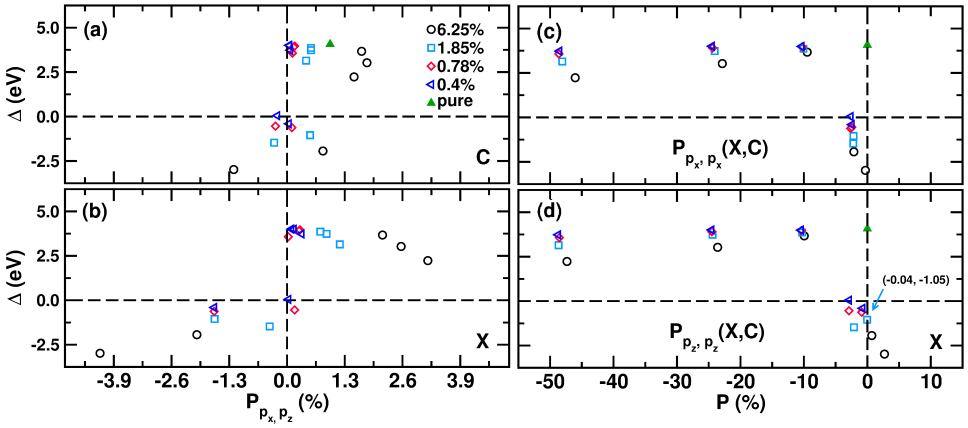


**Figure 3.7:** Generalized band gap as a function of the (a) $\mathcal{P}_{p_x,p_z}(C)$,(b) $\mathcal{P}_{p_x,p_z}(X)$, (c) $\mathcal{P}_{p_x,p_x}$(X,C) and $\mathcal{P}_{p_z,p_z}$(X,C) orbital polarization.

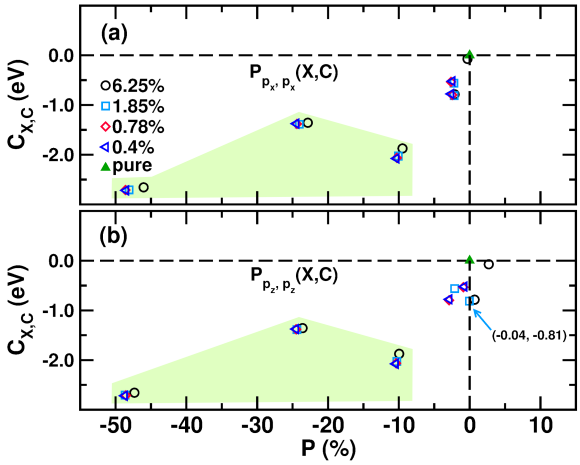


**Figure 3.8:** Bond covalency as a function of the (a) $\mathcal{P}_{p_x,p_x}(X,C)$ and (b) $\mathcal{P}_{p_z,p_z}(X,C)$ orbital polarization. The points included in the shaded area correspond to the systems with positive band gap.

(covalent) the bond character. A possible way to control the ionic character, thus the bang gap width, is by choosing a suitable dopant atomic type.

We can interpret these results in the following way. An ionic character of the X-C bond favours the opening of the (positive) band gap around the Fermi level, while the arrangement of the electron density at the dopant site is responsible for the band gap width. It seems that in general, increasing the amount of charge in the dopant's $p_z$ orbital narrows the band gap width; while increasing the unbalance in favour of the dopant's $p_x$, $p_y$ orbitals appears to open the gap. Therefore, in order to have a positive band gap, the charge accumulation has to be accommodated at the $x$, $y$ plane around the dopant site, whereas an excess of charge along the $z$-axis closes the band gap ($\Delta \leq 0$).

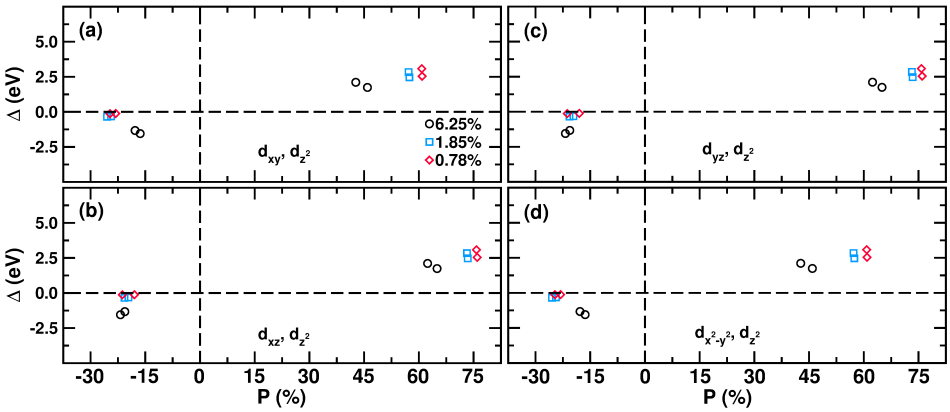


**Figure 3.9:** Generalized band gap as a function of the (a) $\mathcal{P}_{d_{xy},d_{z^2}}(X)$, (b) $\mathcal{P}_{d_{xz},d_{z^2}}(X)$, (c) $\mathcal{P}_{d_{yz},d_{z^2}}(X)$ and (d) $\mathcal{P}_{d_{x^2-y^2},d_{z^2}}(X)$ orbital polarization at the selected dopant concentrations for X = Sc, Ti, V and Cr. The band gap is positive for positive values of the polarization.

We now proceed with the polarization analysis of the structures doped by transition metals in order to test our predictions. In these cases, we conduct the analysis on the $d$ orbitals of the dopant, since they are predominant in the top of the valence band and the bottom of the conduction band. We then consider four different polarizations, namely $\mathcal{P}_{d_{xy},d_{z^2}}(X)$, $\mathcal{P}_{d_{xz},d_{z^2}}(X)$, $\mathcal{P}_{d_{yz},d_{z^2}}(X)$, $\mathcal{P}_{d_{x^2-y^2},d_{z^2}}(X)$. We recall that in the previous section we found that two pairs of orbitals, $d_{xy}$, $d_{x^2-y^2}$ and $d_{xz}$, $d_{yz}$, are degenerate, thus $\mathcal{P}_{d_{xy},d_{z^2}}(X) = \mathcal{P}_{d_{x^2-y^2},d_{z^2}}(X)$ and $\mathcal{P}_{d_{xz},d_{z^2}}(X) = \mathcal{P}_{d_{yz},d_{z^2}}(X)$. We also recall that the most contributing orbital in the bottom of the conduction band is the $d_{z^2}$ orbital, which is occupied in the systems doped by Cr and V, i.e., the systems with the negative band gap. This is consistent with our previous observations: a positive band gap exists in the systems in which the charge is predominantly accommodated in the $x, y$ plane. In fact, the band gap is positive whenever $\mathcal{P}_{d_{xy},d_{z^2}}(X)$, $\mathcal{P}_{d_{x^2-y^2},d_{z^2}}(X)$, $\mathcal{P}_{d_{xz},d_{z^2}}(X)$, $\mathcal{P}_{d_{yz},d_{z^2}}(X)$ are also positive (Figure 3.9). This is again in good agreement with our observation: the excess of charge along the $z$-axis passing through the dopant site is responsible for the negative band gap.

In some applications, we might need to use dopants which would promote the metallic properties of the system, but we still want to have a positive band gap. In the cases like this, the imposition of suitable axial strains may encourage the redistribution of the charge to cause its excess in the $x, y$ plane. It has already been proved that lattice strains can induce charge transfer among the orbitals and promote metal-insulator transitions [11, 32, 17, 16, 58]. To this aim, we consider the N-2 system as an example and apply a 15% axial strain along all three crystallographic axes. By analysing the band structure (Figure 3.10a), we observe that an indirect band gap ($W \to \Gamma$) of about 0.6 eV emerges above the Fermi level. By inspecting the DOS projected on the

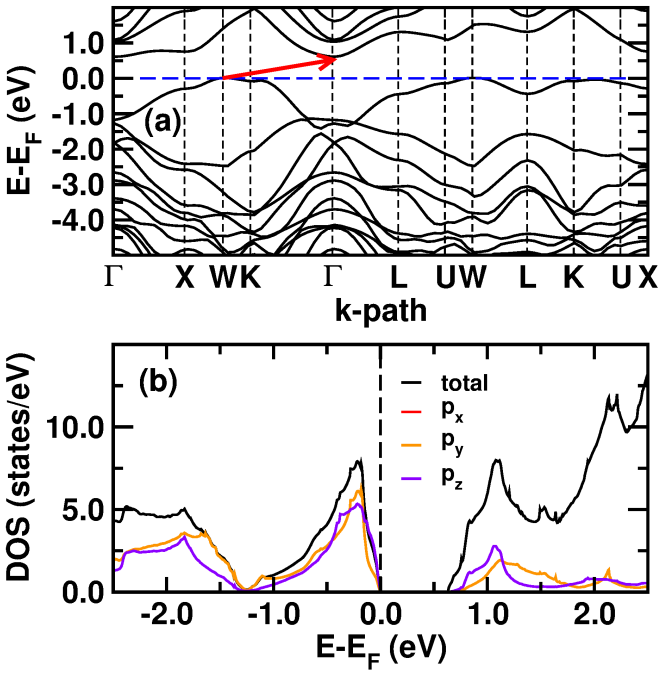


**Figure 3.10:** (a) Electronic band dispersion and (b) N-projected density of states of the N-doped system at 6.25%. The applied strain favours an accumulation of charge in the $x, y$ plane and, therefore, the opening of a band gap. The Fermi level has been set to 0 eV.

atomic site of the dopant (Figure 3.10b), we indeed find the increase in the contribution of the $p_x$ and $p_y$ orbitals at the top of the valence band when compared to the non-strained case. In fact, the application of the strain caused an increase of 2.2% of the $\mathcal{P}_{p_x,p_z}(X)$ $(= \mathcal{P}_{p_y,p_z}(X))$ polarization, which allowed the opening of the band gap.

## 3.5 How to Engineer the Character of the Band Gap

In section 2.6, we discussed that another property of the band gap is its character (*directness*), besides its width. We remind that the band gap is called *direct* when the valence band maximum (VBM) and the conduction band minimum (CBM) are located at the same $\boldsymbol{k}$ vector ($\boldsymbol{k}_{VBM} = \boldsymbol{k}_{CBM}$). On the other hand, when VBM and CBM are located at different $\boldsymbol{k}$ vectors ($\boldsymbol{k}_{VBM} \neq \boldsymbol{k}_{CBM}$) the band gap is *indirect*. The band gap character plays a fundamental role in the optical characteristics of photo-active materials, especially in the efficiency of photovoltaic devices [52]. It is then worthy to

identify the physical properties governing the bad gap character. To this aim, in this section we will consider only the systems with positive band gap ($\Delta \geq 0$), namely doped by Al, B, Si, Sc and Ti.

We observe that regardless of the atomic type of the p-block dopant, the band gap is realised between the VBM located at $\Gamma$ ($\boldsymbol{k}_{VBM} = (0,0,0)$) and the CBM the location of which ($\boldsymbol{k}_{CBM}$) depends solely on the size of the system, thus on the concentration of the dopant. According to this observation, we can assume that the character of the bandgap is determined by the geometry of the system. At the moment, we are not successful in finding any published theoretical description presenting a connection between the character of the band gap, the geometry of the structure and the atomic types forming the latter. Existing works taking into account electronegativity, the electronic structure and systems' symmetries are based on statistical observations or on linear combinations of the atomic orbitals [56, 51]. However, in order to obtain the information about the band gap character, the lack of unified theory makes it mandatory to calculate the band structure of the individual systems. In this section, we will try to formulate a general description which can be applied to periodic systems with any chemical composition and structural geometry.

| X | 2 (6.25%) | 3 (1.85%) | 4 (0.78%) | 5 (0.4%) |
|---|---|---|---|---|
| Al | $\approx 1/4$ | 0 | $1/2$ | 0.1 |
| B | $\approx 1/4$ | 0 | $1/2$ | 0 |
| Si | $\approx 1/4$ | 0 | $1/2$ | 0.1 |
| Sc | $1/2$ | $1/2$ | 0.3182 | · |
| Ti | $1/2$ | $1/2$ | 0 | · |
| Exp. | $1/4$ | $1/12$ | $1/2$ | 0.05 |

**Table 3.2:** Calculated $\boldsymbol{k}_{CBM}$ points which realize the band gap. The numeric label of the columns indicates the multiplicity of the system, whereas the corresponding dopant concentration is reported in parentheses. The components of such points are of the form $\boldsymbol{k}_{CBM} = (\xi, 0, \xi)$; we here report only the $\xi$ value for simplicity. The row labelled as "Exp." shows the expected values calculated from the folding considerations. In the pure system, $\boldsymbol{k}_{CBM} = \boldsymbol{k}^* = (3/8, 0, 3/8)$.

### 3.5.1 Band Folding

In all the considered doped systems, irrespective of the atomic type or the concentration, we encounter the same space group $F\bar{4}3m$. Moreover, we observe that the character of the band gap depends on the unit cell

multiplicity. As a result, we do not expect the symmetries to play a role in determining the directness of the gap, hence we can exclude them from our search and focus on the dimensionality of the system. To this aim, we resort to the concept of *band folding* and how the superlattice arrangement affects the location of the VBM and CBM [41, 61].

The *band folding* is a concept emerging from the use of the supercells, i.e., cells created by replication of the primitive cell. The supercells are commonly used to simulate structures where the translation symmetry of the underlying matrix is broken, such as in doped structures, structures with lattice distortions or magnetic systems. However, when we increase the size of the vectors of the direct lattice, we reduce the size of the reciprocal vectors according to Equation 2.26 (subsection 2.4.2), thus the size of the first Brillouin zone in the reciprocal space shrinks. In turn, the bands in the first Brillouin zone of the primitive cell are remapped ("folded") into the smaller Brillouin zone of the supercell, resulting in a much more populated band structure [42]. We indeed simulate different dopant concentrations by replicating the undoped structure and substituting one carbon atom with a dopant. In this way, the supercell becomes the primitive unit cell of the doped system. However, as we substitute only one carbon atom, the band structure of the supercell is very reminiscent of the pure structure. This results in the folding of the pristine bands according to the number of replicas of the pure structure in the supercell. In the pristine structure, the smallest band gap about the Fermi level is realized between the VBM is located at Γ and the CBM is located at $\boldsymbol{k}_{CBM} = \boldsymbol{k}^* = (3/8, 0, 3/8)$. The Γ point (and therefore the VBM) is left unvaried irrespective of the multiplicity of the supercell, as it is always remapped onto itself. However, the location of the CBM ($\boldsymbol{k}^*$) is always remapped onto the different $\boldsymbol{k}_{CBM}$ depending on the multiplicity of the system. We report the observed $\boldsymbol{k}_{CBM}$ in the Table 3.2 alongside the expected $\boldsymbol{k}_{exp}$, which we calculate by considering the band folding. The process of calculating the expected location of the CBM can be explained on the X-2 systems. We will here discuss only one of the non-null components of the $\boldsymbol{k}_{exp}$ vector, as it has the form $\boldsymbol{k}_{exp} = (\xi, 0, \xi)$ (Table 3.2). Let's consider $1/2$ as the reference point in the pristine structure as it is remapped onto the Γ in the X-2 system. In a primitive system, the distance between the $3/8$ and the reference point $1/2$ is $3/8$-$1/2$=-$1/8$. By rescaling such distance by $1/2$, which is the length of half of the BZ, the vector $(3/8, 0, 3/8)$ is remapped onto $(-1/4, 0, -1/4)$, which is equivalent to $(1/4, 0, 1/4)$. The calculation for the other systems proceeds analogously.

If we examine the table, we find that the values expected from refolding considerations are similar to those observed in the case of Al-, B- and Si-doped structures. This suggests that a feasible way to control the character of the band gap is to exploit the band folding via imposing the desired multiplicity of the cell, in other words, by choosing a suitable concentration of the dopant.

The calculated and observed values are in good agreement in the cases where the orbitals with which the dopant contributes to the band structure around the band gap the most are of $p$ kind, thus the same kind of orbitals of the host matrix (carbon atoms in our case). In the cases doped by transition metals, the situation is complicated by the presence of the $d$ orbitals, which hybridise with the carbon's $p$ orbitals in a more complex way. Such a complexity emerges from the interplay between the symmetries of the involved orbitals and of the bands forming the band gap [80]. Consequently, the reference vector $\boldsymbol{k}^*$ which is remapped onto the supercell's CBM is no longer the one of the pristine structure and does not match the one predicted by the band folding. Moreover, in these cases, not even the VBM is located at the $\Gamma$. As the derivation of the reference vector $\boldsymbol{k}^*$ is not trivial in this latter case, we will not try to find a way to calculate it in this work; however, it will be the subject of our future investigations.

We found out that we can modify and fix the character of the band gap by choosing a suitable concentration of the dopant, as it dictates the lattice parameters (size) of the primitive cell. Then we can guess that other options modifying the lattice parameters, such as imposing suitable axial strains, would do the same. To this aim, we consider the Al-2, B-2 and Si-2 models and we apply tensile biaxial strains along the $\boldsymbol{a}$ and $\boldsymbol{b}$ crystallographic axes. We then compare systems with 0%, 5% and 10% strain values. We observe that, as the strain increases, the $\boldsymbol{k}_{CBM}$ shifts towards the $\Gamma$ point until it reaches it ($\boldsymbol{k}_{CBM} = \Gamma$) and forms a direct band gap (Figure 3.11). We again find that such behaviour does not depend on the atomic type of the dopant but only on the lattice parameters of the primitive unit cell.

We would like to emphasize that we simulate different dopant concentrations by considering supercells always with one dopant atom. Since the model systems are periodic, the position of the dopant is regularly replicated along the spatial coordinates, thus we always consider ordered homogeneous distributions of the dopant. Therefore, the results presented in this section are relevant to guide the manufacture of energetically efficient photovoltaic devices where a homogeneous dopant distribution has already been proved to improve the material response [71, 33, 64, 40, 35, 79].

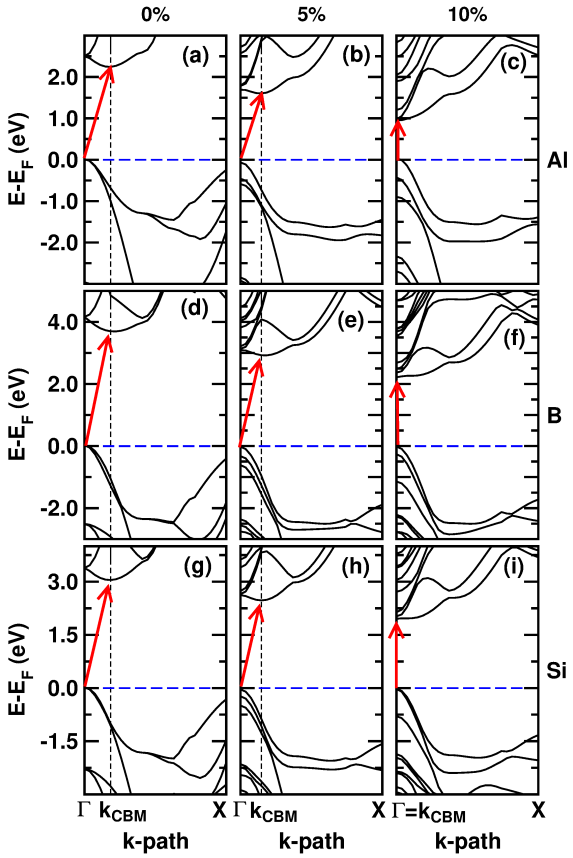


**Figure 3.11:** Electronic band structure of the (a-c) Al-2, (d-f) B-2 and (g-i) Si-2 system at the considered axial strain. The strain value reported at the top of the first three subfigures is common to all the subfigures in the respective columns. As the strain increases, $\boldsymbol{k}_{CBM}$ is shifted towards the origin of the Brillouin zone, until a direct band gap is realized at $\boldsymbol{k}_{CBM} = \Gamma$. The Fermi level has been set to 0 eV.

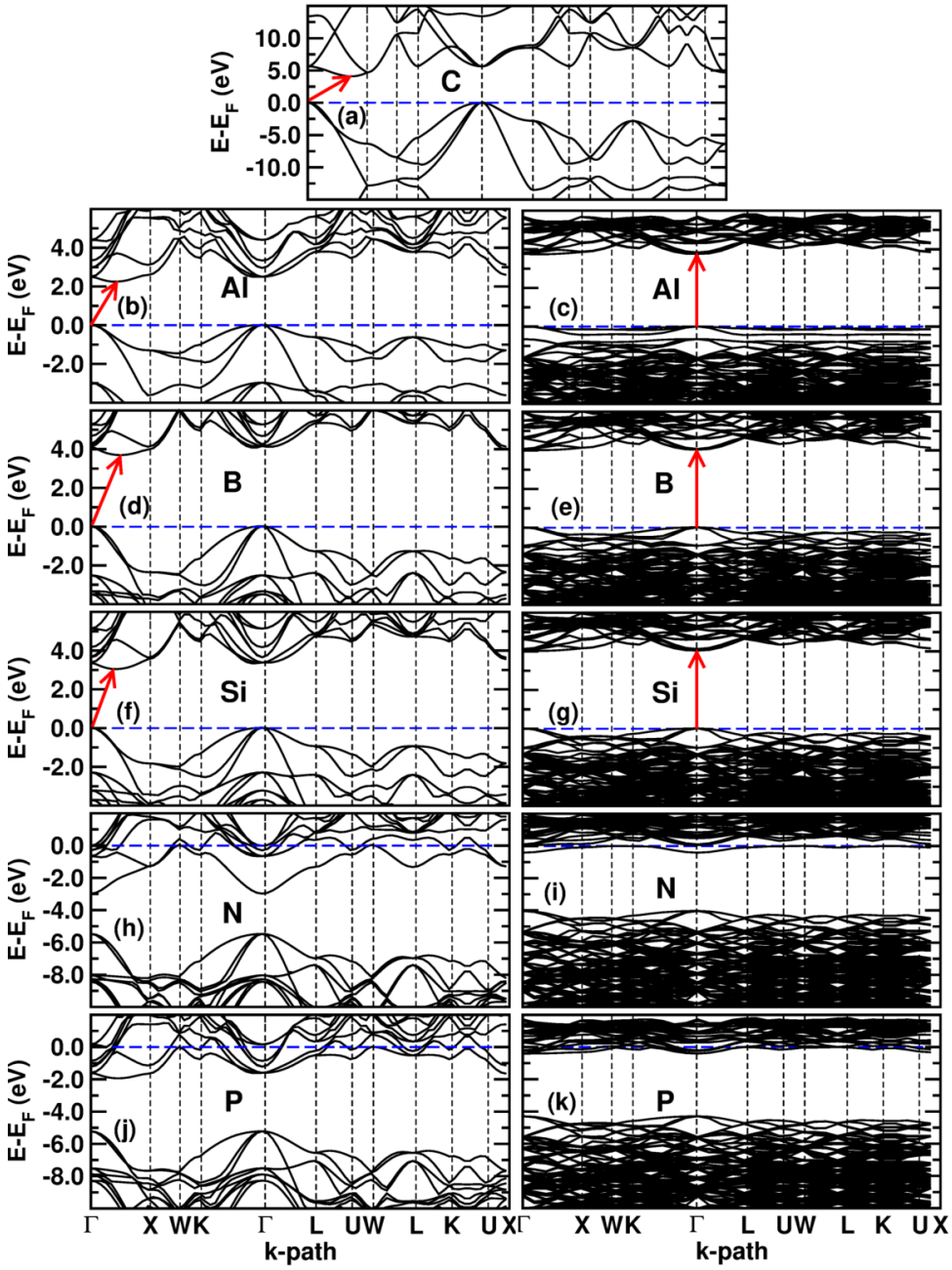


**Figure 3.12:** Electronic band structure of the pure diamond (a), Al- (b, c), B- (d, e), Si- (e, f), N-(g, h) and P-doped (i, j) structures. The plots on the left corresponds to the X-2 systems while the plots on the right to the X-5. The blue line represents the Fermi level set to 0.0 eV, while the red arrow shows the electronic transition to overcome the band gap.

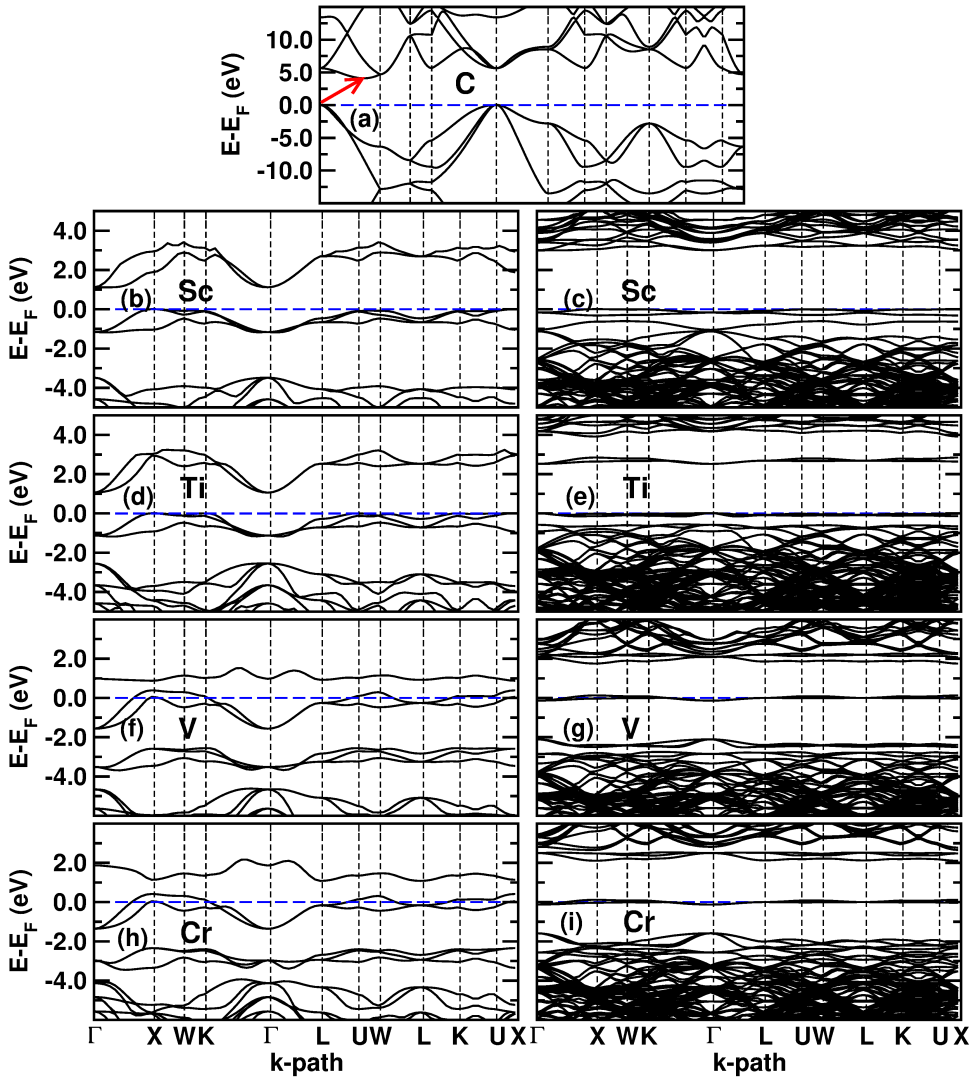


**Figure 3.13:** Electronic band structure of the pure diamond (a), Sc (b, c) , Ti (d, e), V (f, g) and Cr-doped (h, i) structures. The plots on the left correspond to the X-2 systems while the plots on the right to the X-4. The blue line represents the Fermi level set to 0.0 eV.

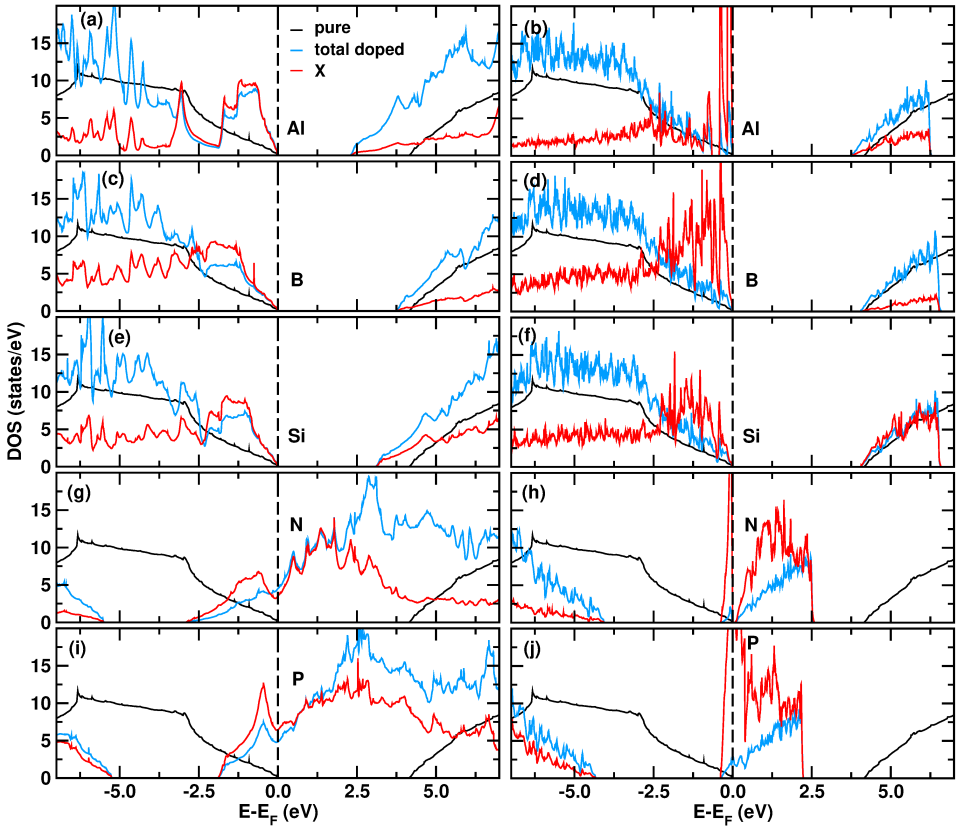


**Figure 3.14:** Density of states of (a) Al-, (b) B-, (c) Si-, (d) N- and (e) P-doped systems. The plots on the left correspond to the X-2 systems while the plots on the right to the X-5. The "pure" and "total" labels indicate the total density of states of the pure diamond and the doped system, respectively, while the "X" label indicates the density of states projected on the atomic site of the dopant corresponding to the atomic symbol in the plot. For clarity of presentation, the total DOS plots are normalized by the number of cell replicas while the projected DOS are reported as calculated. The Fermi level is set at 0 eV and is indicated by the vertical dashed lines.

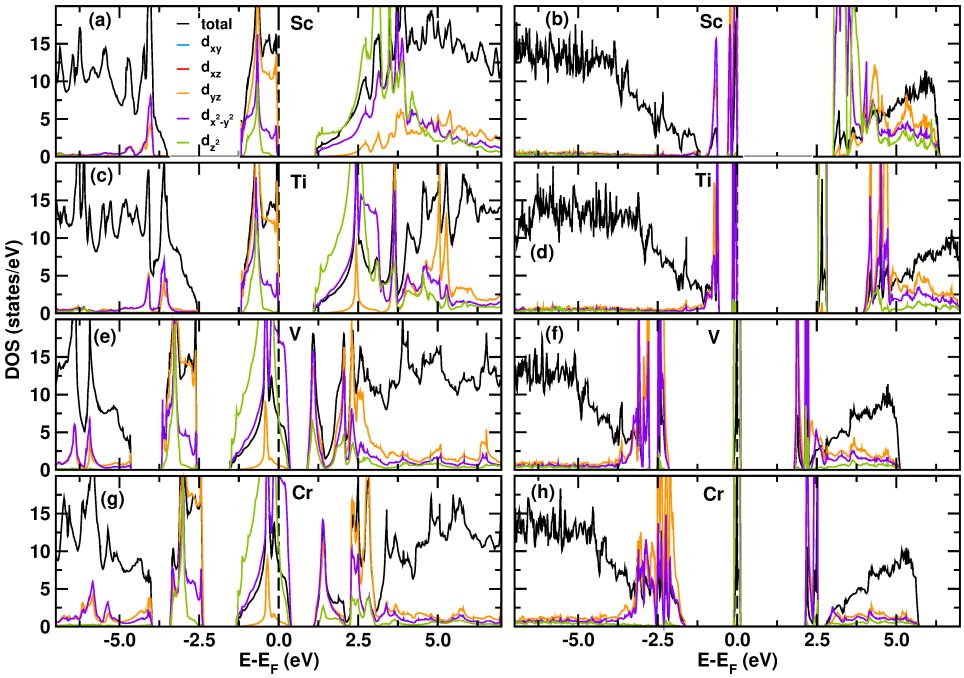


**Figure 3.15:** Density of states resolved for the d-orbitals centered at the dopant site for the (a-b) Sc-, (c-d) Ti-, (e-f) V and Cr-doped (g-h) systems. The plots on the left corresponds to the X-2 systems while the plots on the right to the X-4. The blue line represents the Fermi level set to 0.0 eV. The pairs of orbitals $d_{xy}$, $d_{yz}$ and $d_{xz}$, $d_{x^2-y^2}$ are degenerate, thus ther corresponding curves are overlapping. The "total" label refers to the total density of states which has been normalized by the number of cell replicas.

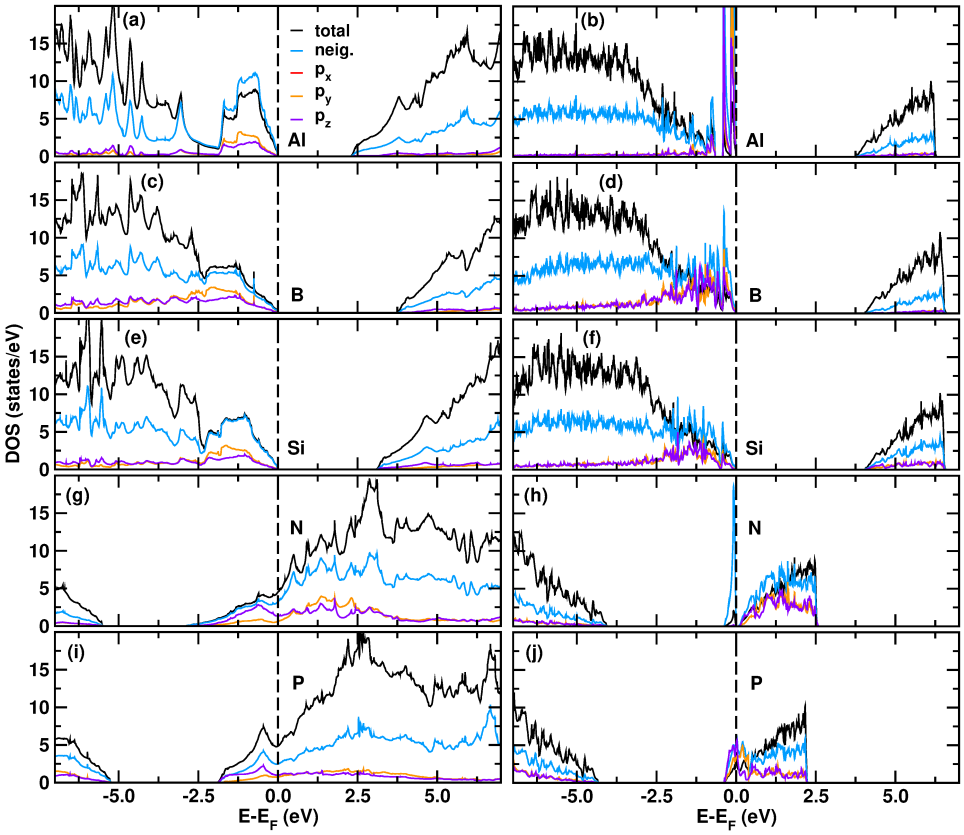


**Figure 3.16:** Density of states resolved for the $p_x$, $p_y$ and $p_z$ orbitals centered at the dopant site for the (a-b) Al-, (c-d) B-, (e-f) Si, (g-h) N- and (i-j) P-doped systems. The plots on the left correspond to the X-2 systems while the plots on the right to the X-5. The $p_x$ and $p_y$ orbitals are degenerate and the corresponding curves overlap in each subplot. The "total" label refers to the total density of states which has been normalized by the number of cell replicas; the data labelled as "neig." corresponds to the density of states projected onto any of the four nearest neighbouring carbon atoms surrounding the substituent. The Fermi level is set at 0.0 eV and is indicated by the vertical dashed lines.

# Chapter 4

# Conclusions

In the presented work, we studied how to tune the width and the character of the band gap in diamond-based materials. To this aim, we conducted quantum mechanical simulations of diamond-derived systems created by considering a large variety of dopants at different concentrations.

The atomic type of the dopant does not determine the symmetries of the system, as it forms a regular tetrahedron with the carbon atoms in its first coordination shell; nonetheless, it governs the subtle features of electronic distribution in its local environment. We found that the bond covalency between the dopant and the surrounding carbon atoms seems to be a viable parameter to regulate the size of the band gap. Increasing values of the bond covalency narrow the band gap until a certain threshold is reached, then the band gap disappears and the system becomes metallic. The bond covalency is determined by the local distributions of the electronic density. We analysed such distributions by means of the orbital polarization analysis. The analysis showed that if the charge is preferentially accommodated in the $x, y$ plane then a band gap is present, while an increase of electronic charge along the $z$-axis narrows its width. On the other hand, the band gap ceases to exist when the charge along the $z$-axis becomes predominant with respect to the that on the $x, y$ plane. Therefore, it is possible to promote desired charge redistributions by choosing suitable dopant atomic types or by imposing axial strains with the aim of obtaining the desired band gap value. We proved these findings also with the use of transition metal dopants; this indeed widens the possible applications of diamond based materials where the transition metals are required for their electron-correlation properties. Moreover, we demonstrated that we can induce the presence of a band gap even in the case of $n$-type doping.

We found that the directness of the band gap is determined solely by the dimensionality of the system, i.e., by the concentration of the dopant. The concentration dictates the size of the primitive unit cell in terms of a precise number of replicas of the undoped structure. This causes the reminiscence of the band structure of the supercell and the pristine band structure. As a result, the reciprocal vectors of the pristine structure realizing the smallest band gap are remapped onto different vectors of superlattice structure. The ramapping happens according to the unit cell multiplicity in the process known as band folding. We, therefore, understood that the length of the lattice parameters is crucial in determining the directness of the band gap. Then, we can induce an indirect-to-direct transformation by modifying the lattice parameters of the system. We demonstrated that such a modification can be obtained at a fixed dopant type not only by choosing suitable concentrations but also by applying proper biaxial strains.

The results presented in this thesis can serve as guidelines on how to choose dopant atomic types and concentrations to engineer the band gap size, and how to act on the lattice parameters to achieve a suitable band gap character in diamond-based systems. Our theoretical results and used approach are general and therefore can be applied to the design of materials far beyond those based on diamond or containing the dopants considered in this study. We would like to expand the presented study and continue the investigation of the diamond-based materials in the future. Indeed, we already started to work on a project which considers different geometric arrangements of the dopants and vacancies in the diamond supercells.

The results of this work were presented at the American Physical Society March Meeting 2022 (Chicago, IL, USA) as well as reported in the scientific article which is under review at the time of the thesis composition.

# Appendix A

## Bibliography


[1] Carlo Adamo and Vincenzo Barone. Toward reliable density functional methods without adjustable parameters: The pbe0 model. *The Journal of Chemical Physics*, 110(13):6158–6170, 1999.

[2] T. Astner, J. Gugler, A. Angerer, S. Wald, S. Putz, N. J. Mauser, M. Trupke, H. Sumiya, S. Onoda, J. Isoya, J. Schmiedmayer, P. Mohn, and J. Majer. Solid-state electron spin lifetime limited by phononic vacuum modes. *Nat. Mater.*, 17(4):313–317, Apr 2018.

[3] Peter Atkins and Ronald Friedman. *Molecular Quantum Mechanics*. Oxford University Press Inc., 2005.

[4] Axel D. Becke. A new mixing of hartree-fock and local density functional theories. *The Journal of Chemical Physics*, 98(2):1372–1377, 1993.

[5] Florian Belviso, Victor E. P. Claerbout, Aleix Comas-Vives, Naresh S. Dalal, Feng-Ren Fan, Alessio Filippetti, Vincenzo Fiorentini, Lucas Foppa, Cesare Franchini, Benjamin Geisler, Luca M. Ghiringhelli, Axel Groß, Shunbo Hu, Jorge Íñiguez, Steven Kaai Kauwe, Janice L. Musfeldt, Paolo Nicolini, Rossitza Pentcheva, Tomas Polcar, Wei Ren, Fabio Ricci, Francesco Ricci, Huseyin Sener Sen, Jonathan Michael Skelton, Taylor D. Sparks, Alessandro Stroppa, Andrea Urru, Matthias Vandichel, Paolo Vavassori, Hua Wu, Ke Yang, Hong Jian Zhao, Danilo Puggioni, Remedios Cortese, and Antonio Cammarata. Viewpoint: Atomic-scale design protocols toward energy, electronic, catalysis, and sensing applications. *Inorg. Chem.*, 58(22):14939–14980, 2019.

[6] Niels Bindzus, Tine Straasø, Nanna Wahlberg, Jacob Becker, Lasse Bjerg, Nina Lock, Ann-Christin Dippel, and Bo B. Iversen. Experimental

determination of core electron deformation in diamond. *Acta Crystallogr. A*, 70(1):39–48, Jan 2014.

[7] V. D. Blank, K. N. Boldyrev, V. N. Denisov, V. V. Denisov, A. S. Galkin, M. S. Kuznetsov, B. N. Mavrin, S. A. Nosukhin, D. D. Prikhodko, A. A. Sukhanov, S. A. Tarelkin, and S. A. Terentiev. Electronic band structure of phosphorus-doped single crystal diamond: Dynamic jahn-teller distortion of the tetrahedral donor ground state. *Phys. Rev. B*, 102:115153, Sep 2020.

[8] M. Born and R. Oppenheimer. Zur Quantentheorie der Molekeln. *Annalen der Physik*, 389(20):457–484, January 1927.

[9] Antonio Cammarata and Tomas Polcar. Electro-vibrational coupling effects on "intrinsic friction" in transition metal dichalcogenides. *RSC Adv.*, 5:106809–106818, 2015.

[10] Antonio Cammarata and Tomas Polcar. Layering effects on low frequency modes in $n$-layered $MX_2$ transition metal dichalcogenides. *Phys. Chem. Chem. Phys.*, 18:4807–4813, 2016.

[11] Antonio Cammarata and James M. Rondinelli. Octahedral engineering of orbital polarizations in charge transfer oxides. *Phys. Rev. B*, 87:155135, Apr 2013.

[12] Antonio Cammarata and James M. Rondinelli. Covalent dependence of octahedral rotations in orthorhombic perovskite oxides. *J. Chem. Phys.*, 141(11):114704, 2014.

[13] Stefania Castelletto, Lorenzo Rosa, Jonathan Blackledge, Mohammed Zaher Al Abri, and Albert Boretti. Advances in diamond nanofabrication for ultrasensitive devices. *Microsystems & Nanoengineering*, 3(1):17061, Oct 2017.

[14] Paul R. Chalker. Wide bandgap semiconductor materials for high temperature electronics. *Thin Solid Films*, 343-344:616–622, 1999.

[15] Jianwei Che, Tahir Çağın, Weiqiao Deng, and William A. Goddard. Thermal conductivity of diamond and related materials from molecular dynamics simulations. *J. Chem. Phys.*, 113(16):6888–6900, 2000.

[16] Binbin Chen, Nicolas Gauquelin, Robert J. Green, Jin Hong Lee, Cinthia Piamonteze, Matjaž Spreitzer, Daen Jannis, Johan Verbeeck, Manuel Bibes, Mark Huijben, Guus Rijnders, and Gertjan Koster. Spatially controlled octahedral rotations and metal–insulator transitions in nickelate superlattices. *Nano Lett.*, 21(3):1295–1302, 2021.

[17] Binbin Chen, Nicolas Gauquelin, Daen Jannis, Daniel M. Cunha, Ufuk Halisdemir, Cinthia Piamonteze, Jin Hong Lee, Jamal Belhadi, Felix Eltes, Stefan Abel, Zoran Jovanović, Matjaž Spreitzer, Jean Fompeyrine,

Johan Verbeeck, Manuel Bibes, Mark Huijben, Guus Rijnders, and Gertjan Koster. Strain-engineered metal-to-insulator transition and orbital polarization in nickelate superlattices integrated on silicon. *Adv. Mater.*, 32(50):2004995, 2020.

[18] Sujit Das, Laura D. Marlino, and Kristina O. Armstrong. Wide bandgap semiconductor opportunities in power electronics. 1 2018.

[19] C. David Sherrill and Henry F. Schaefer. The configuration interaction method: Advances in highly correlated approaches. volume 34 of *Advances in Quantum Chemistry*, pages 143 – 269. Academic Press, 1999.

[20] Zhou Delun, Lin Tang, Yiwen Geng, Jinyu Zhang, Ruifeng Yue, and Yan Wang. First-principles calculation to n-type lin co-doping and li doping in diamond. *Diamond and Related Materials*, 110:108070, 2020.

[21] D. Eon, A. Traoré, J. Pernot, and E. Gheeraert. Recent progress on diamond schottky diode. In *2016 28th International Symposium on Power Semiconductor Devices and ICs (ISPSD)*, pages 55–58, June 2016.

[22] R. P. Feynman. Forces in molecules. *Phys. Rev.*, 56:340–343, Aug 1939.

[23] V. Fock. Näherungsmethode zur lösung des quantenmechanischen mehrkörperproblems. *Zeitschrift für Physik*, 61:126–148, 1930.

[24] Shang-Peng Gao. Band gaps and dielectric functions of cubic and hexagonal diamond polytypes calculated by many-body perturbation theory. *physica status solidi (b)*, 252, 09 2014.

[25] C. Giacovazzo. *Fundamentals of Crystallography*. Oxford University Press Inc., 1992.

[26] Xavier Gonze, Bernard Amadon, Gabriel Antonius, Frédéric Arnardi, Lucas Baguet, Jean-Michel Beuken, Jordan Bieder, François Bottin, Johann Bouchet, Eric Bousquet, Nils Brouwer, Fabien Bruneval, Guillaume Brunin, Théo Cavignac, Jean-Baptiste Charraud, Wei Chen, Michel Côté, Stefaan Cottenier, Jules Denier, Grégory Geneste, Philippe Ghosez, Matteo Giantomassi, Yannick Gillet, Olivier Gingras, Donald R. Hamann, Geoffroy Hautier, Xu He, Nicole Helbig, Natalie Holzwarth, Yongchao Jia, François Jollet, William Lafargue-Dit-Hauret, Kurt Lejaeghere, Miguel A. L. Marques, Alexandre Martin, Cyril Martins, Henrique P. C. Miranda, Francesco Naccarato, Kristin Persson, Guido Petretto, Valentin Planes, Yann Pouillon, Sergei Prokhorenko, Fabio Ricci, Gian-Marco Rignanese, Aldo H. Romero, Michael Marcus Schmitt, Marc Torrent, Michiel J. van Setten, Benoit Van Troeye, Matthieu J. Verstraete, Gilles Zérah, and Josef W. Zwanziger. The abinit project: Impact, environment and recent developments. *Comput. Phys. Commun.*, 248:107042, 2020.

[27] M. J. Han, C. A. Marianetti, and A. J. Millis. Chemical control of orbital polarization in artificially structured transition-metal oxides: $La_2nixo_6$ ($x$ = b, al, ga, in) from first principles. *Phys. Rev. B*, 82:134408, Oct 2010.

[28] D. R. Hartree. The wave mechanics of an atom with a non-coulomb central field. part i. theory and methods. *Mathematical Proceedings of the Cambridge Philosophical Society*, 24(1):89–110, 1928.

[29] Jochen Heyd, Gustavo E. Scuseria, and Matthias Ernzerhof. Hybrid functionals based on a screened Coulomb potential. *J. Chem. Phys.*, 118(18):8207–8215, May 2003.

[30] Steffen Heyer, Wiebke Janssen, Stuart Turner, Ying-Gang Lu, Weng Siang Yeap, Jo Verbeeck, Ken Haenen, and Anke Krueger. Toward deep blue nano hope diamonds: heavily boron-doped diamond nanoparticles. *ACS Nano*, 8(6):5757–5764, June 2014.

[31] F. L. Hirshfeld. Bonded-atom fragments for describing molecular charge densities. *Theor. Chim. Acta*, 44(2):129–138, Jun 1977.

[32] Bin Hong, Yuanjun Yang, Kai Hu, Yongqi Dong, Jingtian Zhou, Yue Zhang, Weisheng Zhao, Zhenlin Luo, and Chen Gao. Strain engineering on the metal-insulator transition of $vo_2/tio_2$ epitaxial films dependent on the strain state of vanadium dimers. *Appl. Phys. Lett.*, 115(25):251605, 2019.

[33] Masahiro Hori, Takahiro Shinada, Yukinori Ono, Akira Komatsubara, Kuninori Kumagai, Takashi Tanii, Tetsuo Endoh, and Iwao Ohdomari. Impact of a few dopant positions controlled by deterministic single-ion doping on the transconductance of field-effect transistors. *Appl. Phys. Lett.*, 99(6):062103, 2011.

[34] J Isberg, J Hammersberg, D.J Twitchen, and A.J Whitehead. Single crystal diamond for electronic applications. *Diam. Relat. Mater.*, 13(2):320 – 324, 2004. Carbon Materials for Active Electronics. Proceedings of Symposium L, E-MRS Spring Meeting 2003.

[35] Shogo Ishizuka and Paul J. Fons. Role of the cu-deficient interface in cu(in,ga)$se_2$ thin-film photovoltaics with alkali-metal doping. *Phys. Rev. Appl.*, 15:054005, May 2021.

[36] W. Kaiser and W. L. Bond. Nitrogen, a major impurity in common type i diamond. *Phys. Rev.*, 115:857–863, Aug 1959.

[37] C. Kittel. *Introduction to Solid State Physics*. John Wiley & Sons Inc., 1971.

[38] Jorge Kohanoff. *Electronic structure calculations for solids and molecules: theory and computational methods*. Cambridge university press, 2006.

[39] W. Kohn and L. J. Sham. Self-Consistent Equations Including Exchange and Correlation Effects. *Physical Review*, 140(4A):1133–1138, November 1965.

[40] Lukas Kranz, Christina Gretener, Julian Perrenoud, Rafael Schmitt, Fabian Pianezzi, Fabio La Mattina, Patrick Blösch, Erik Cheah, Adrian Chirilă, Carolin M. Fella, Harald Hagendorfer, Timo Jäger, Shiro Nishiwaki, Alexander R. Uhl, Stephan Buecheler, and Ayodhya N. Tiwari. Doping of polycrystalline cdte for high-efficiency solar cells on flexible metal foil. *Nat. Commun.*, 4(1):2306, Aug 2013.

[41] Wei Ku, Tom Berlijn, and Chi-Cheng Lee. Unfolding first-principles band structures. *Phys. Rev. Lett.*, 104:216401, May 2010.

[42] Wei Ku, Tom Berlijn, and Chi-Cheng Lee. Unfolding first-principles band structures. *Physical review letters*, 104:216401, 05 2010.

[43] HG Kummel. A biography of the coupled cluster method. volume 17, pages 5311–5325, 11 2003.

[44] N. Lambert, A. Taylor, P. Hubík, J. Bulíř, J. More-Chevalier, H. Karaca, C. Fleury, J. Voves, Z. Šobávn, D. Pogany, and V. Mortet. Modeling current transport in boron-doped diamond at high electric fields including self-heating effect. *Diam. Relat. Mater.*, 109:108003, 2020.

[45] R.M. Martin, R.M. Martin, and Cambridge University Press. *Electronic Structure: Basic Theory and Practical Methods*. Cambridge University Press, 2004.

[46] N. Mizuochi, T. Makino, H. Kato, D. Takeuchi, M. Ogura, H. Okushi, M. Nothaft, P. Neumann, A. Gali, F. Jelezko, J. Wrachtrup, and S. Yamasaki. Electrically driven single-photon source at room temperature in diamond. *Nat. Photonics*, 6(5):299–303, May 2012.

[47] Chr. Møller and M. S. Plesset. Note on an Approximation Treatment for Many-Electron Systems. *Physical Review*, 46(7):618–622, October 1934.

[48] Koichi Momma and Fujio Izumi. *VESTA3* for three-dimensional visualization of crystal, volumetric and morphology data. *Journal of Applied Crystallography*, 44(6):1272–1276, Dec 2011.

[49] Hendrik J. Monkhorst and James D. Pack. Special points for brillouin-zone integrations. *Phys. Rev. B*, 13:5188–5192, Jun 1976.

[50] R. S. Mulliken. Electronic Population Analysis on LCAO-MO Molecular Wave Functions. I. *J. Chem. Phys.*, 23(10):1833–1840, October 1955.

[51] Allen Nussbaum. Crystal symmetry, group theory, and band structure calculations. volume 18 of *Solid State Physics*, pages 165–272. Academic Press, 1966.

[52] Jacques I. Pankove. *Optical Processes in Semiconductors*. Dover Publications, New York, 2010.

[53] W. Pauli. Über den Zusammenhang des Abschlusses der Elektronengruppen im Atom mit der Komplexstruktur der Spektren. *Zeitschrift fur Physik*, 31(1):765–783, February 1925.

[54] John P. Perdew, Stefan Kurth, Ale š Zupan, and Peter Blaha. Accurate density functional with correct formal properties: A step beyond the generalized gradient approximation. *Phys. Rev. Lett.*, 82:2544–2547, Mar 1999.

[55] Gaëtan Perez, Aurélien Maréchal, Gauthier Chicot, Pierre Lefranc, Pierre-Olivier Jeannin, David Eon, and Nicolas Rouger. Diamond semiconductor performances in power electronics applications. *Diam. Relat. Mater.*, 110:108154, 2020.

[56] Padmanabhan Predeep. *Optoelectronics*. IntechOpen, Rijeka, 2011.

[57] Jorne Raymakers, Anna Artemenko, Shannon S. Nicley, Pavla Štenclová, Alexander Kromka, Ken Haenen, Wouter Maes, and Bohuslav Rezek. Expanding the scope of diamond surface chemistry: Stille and sonogashira cross-coupling reactions. *J. Phys. Chem. C*, 121(42):23446–23454, 2017.

[58] Laura Rodríguez, Felip Sandiumenge, Carles Frontera, José Manuel Caicedo, Jessica Padilla, Gustau Catalán, and José Santiso. Strong strain gradients and phase coexistence at the metal-insulator transition in vo2 epitaxial films. *Acta Mater.*, 220:117336, 2021.

[59] E. Rohrer, C. F. O. Graeff, R. Janssen, C. E. Nebel, M. Stutzmann, H. Güttler, and R. Zachai. Nitrogen-related dopant and defect states in cvd diamond. *Phys. Rev. B*, 54:7874–7880, Sep 1996.

[60] C. C. J. Roothaan. New developments in molecular orbital theory. *Rev. Mod. Phys.*, 23:69–89, Apr 1951.

[61] O. Rubel, A. Bokhanchuk, S. J. Ahmed, and E. Assmann. Unfolding the band structure of disordered solids: From bound states to high-mobility kane fermions. *Phys. Rev. B*, 90:115202, Sep 2014.

[62] E. Schrödinger. An undulatory theory of the mechanics of atoms and molecules. *Phys. Rev.*, 28:1049–1070, Dec 1926.

[63] Wahyu Setyawan and Stefano Curtarolo. High-throughput electronic band structure calculations: Challenges and tools. *Computational Materials Science*, 49(2):299 – 312, 2010.

[64] Takahiro Shinada, Shintaro Okamoto, Takahiro Kobayashi, and Iwao Ohdomari. Enhancing semiconductor device performance using ordered dopant arrays. *Nature*, 437(7062):1128–1131, Oct 2005.

[65] J. C. Slater. Note on hartree's method. *Phys. Rev.*, 35:210–211, Jan 1930.

[66] Alexandrina Stoyanova, Alexander O. Mitrushchenkov, Liviu Hozoi, Hermann Stoll, and Peter Fulde. Electron correlation effects in diamond: A wave-function quantum-chemistry study of the quasiparticle band structure. *Phys. Rev. B*, 89:235121, Jun 2014.

[67] T.P. Straatsma, E.J. Bylaska, H.J.J. van Dam, N. Govind, W.A. de Jong, K. Kowalski, and M. Valiev. Chapter 7 - advances in scalable computational chemistry: Nwchem. In Ralph A. Wheeler, editor, *Annual Reports in Computational Chemistry*, volume 7 of *Annual Reports in Computational Chemistry*, pages 151 – 177. Elsevier, 2011.

[68] Hisashi Sumikura, Kazuyuki Hirama, Katsuhiko Nishiguchi, Akihiko Shinya, and Masaya Notomi. Highly nitrogen-vacancy doped diamond nanostructures fabricated by ion implantation and optimum annealing. *APL Mater.*, 8(3):031113, 2020.

[69] Xiang Sun, Yuzheng Guo, Gai Wu, Yan Zhao, Sheng Liu, and Hui Li. Research of n-type arsenic doped diamond: Theoretical analysis of electronic and mechanical properties. *Diamond and Related Materials*, 108:107924, 2020.

[70] Péter G. Szalay, Thomas Müller, Gergely Gidofalvi, Hans Lischka, and Ron Shepard. Multiconfiguration self-consistent field and multireference configuration interaction methods and applications. *Chemical Reviews*, 112(1):108–181, 2012. PMID: 22204633.

[71] Yabing Tang, Baojun Lin, Hanzhang Zhao, Tao Li, Wei Ma, and Han Yan. Significance of dopant/component miscibility to efficient n-doping in polymer solar cells. *ACS Appl. Mater. Inter.*, 12(11):13021–13028, 2020.

[72] Mahtab Ullah, Ejaz Ahmed, Fayyaz Hussain, Anwar Manzoor Rana, Rizwan Raza, and Hafeez Ullah. Electronic structure calculations of oxygen-doped diamond using dft technique. *Microelectronic Engineering*, 146:26–31, 2015. Nanostructured Materials and Green Nanotechnology for future Electronics, photonics, and Nanosystems 2014.

[73] Danny E. P. Vanpoucke, Patrick Bultinck, and Isabel Van Driessche. Extending hirshfeld-i to bulk and periodic materials. *Journal of Computational Chemistry*, 34(5):405–417, February 2013.

[74] James L. Webb, Joshua D. Clement, Luca Troise, Sepehr Ahmadi, Gustav Juhl Johansen, Alexander Huck, and Ulrik L. Andersen. Nanotesla sensitivity magnetic field sensing using a compact diamond nitrogen-vacancy magnetometer. *Appl. Phys. Lett.*, 114(23):231103, 2019.

[75] Chris J.H. Wort and Richard S. Balmer. Diamond as an electronic material. *Mater. Today*, 11(1):22–28, 2008.

[76] Zhigang Wu and R. E. Cohen. More accurate generalized gradient approximation for solids. *Phys. Rev. B*, 73(23), June 2006.

[77] Sadanori Yamanaka, Hideyuki Watanabe, Shigeo Masai, Daisuke Takeuchi, Hideyo Okushi, and Koji Kajimura. High-quality b-doped homoepitaxial diamond films using trimethylboron. *Jpn. J. Appl. Phys.*, 37(Part 2, No. 10A):L1129–L1131, oct 1998.

[78] Cui Xia Yan, Ying Dai, and Bai Biao Huang. DFT study of halogen impurity in diamond. *Journal of Physics D: Applied Physics*, 42(14):145407, jun 2009.

[79] Zi-Jun Yong, Shao-Qiang Guo, Ju-Ping Ma, Jun-Ying Zhang, Zhi-Yong Li, Ya-Meng Chen, Bin-Bin Zhang, Yang Zhou, Jie Shu, Jia-Li Gu, Li-Rong Zheng, Osman M. Bakr, and Hong-Tao Sun. Doping-enhanced short-range order of perovskite nanocrystals for near-unity violet luminescence quantum yield. *J. Am. Chem. Soc.*, 140(31):9942–9951, 2018.

[80] Lin-Ding Yuan, Hui-Xiong Deng, Shu-Shen Li, Su-Huai Wei, and Jun-Wei Luo. Unified theory of direct or indirect band-gap nature of conventional semiconductors. *Phys. Rev. B*, 98:245203, Dec 2018.

# MASTER‘S THESIS ASSIGNMENT

## I. Personal and study details

Student's name: **Kaintz Matúš** Personal ID number: **474677**

Faculty / Institute: **Faculty of Electrical Engineering**

Department / Institute: **Department of Control Engineering**

Study program: **Cybernetics and Robotics**

Branch of study: **Cybernetics and Robotics**

## II. Master’s thesis details

Master’s thesis title in English:

**Structural tuning of band gap in nanostructured diamonds**

Master’s thesis title in Czech:

**Strukturní ladění zakázaného pásma v nanostrukturovaných diamantech**

Guidelines:

The goal of the present study is to extend the acquired knowledge on quantum mechanics and ab initio softwares. As an application, the candidate will study how to design diamond-based nanostructures with targeted band gap values. The presence of dopant atoms in combination with vacancies will be considered, in order to understand the coupled structural-electronic features governing the electronic properties of each system, and finally the band gap. The topic is in line with the state of the art of the research for new materials for electronic applications. In this respect, diamond has already been recognized to have great potentials in devices such as high-frequency field-effect transistors, high-power switches and Schottky diodes.

Bibliography / sources:

[1] Peter Atkins and Ronald Friedman – Molecular Quantum Mechanics (Fifth Edition) – online – ISBN-10: 0199541426, Oxford University Press, 2011
[2] Charles Kittel – Introduction to Solid State Physics (Eigth Edition) – online – ISBN-10: 047141526X, Wiley, 2004
[3] Claude Cohen-Tannoudji, Bernard Diu, Franck Laloë – Quantum Mechanics, Volume 1: Basic Concepts, Tools, and Applications (Second Edition) – online – ISBN-13: 9783527345533, Wiley-VCH, 2019

Name and workplace of master’s thesis supervisor:

**Antonio Cammarata, Ph.D. Department of Control Engineering FEE**

Name and workplace of second master’s thesis supervisor or consultant:

Date of master’s thesis assignment: **15.11.2021** Deadline for master's thesis submission: **20.05.2022**

Assignment valid until:
**by the end of summer semester 2022/2023**

| Antonio Cammarata, Ph.D. | prof. Ing. Michael Šebek, DrSc. | prof. Mgr. Petr Páta, Ph.D. |
|---|---|---|
| Supervisor’s signature | Head of department’s signature | Dean’s signature |

## III. Assignment receipt

The student acknowledges that the master’s thesis is an individual work. The student must produce his thesis without the assistance of others, with the exception of provided consultations. Within the master’s thesis, the author must state the names of consultants and include a list of references.

| Date of assignment receipt | Student’s signature |
|---|---|